

# NLO QCD and electroweak corrections to $W + \gamma$ production with leptonic W-boson decays

ANSGAR DENNER<sup>1</sup>, STEFAN DITTMAIER<sup>2</sup>, MARKUS HECHT<sup>2</sup>, CHRISTIAN PASOLD<sup>1</sup>

<sup>1</sup>*Julius-Maximilians-Universität Würzburg, Institut für Theoretische Physik und Astrophysik,  
D-97074 Würzburg, Germany*

<sup>2</sup>*Albert-Ludwigs-Universität Freiburg, Physikalisches Institut,  
D-79104 Freiburg, Germany*

## Abstract:

We present a calculation of the next-to-leading-order electroweak corrections to  $W + \gamma$  production, including the leptonic decay of the W boson and taking into account all off-shell effects of the W boson, where the finite width of the W boson is implemented using the complex-mass scheme. Corrections induced by incoming photons are fully included and find particular emphasis in the discussion of phenomenological predictions for the LHC. The corresponding next-to-leading-order QCD corrections are reproduced as well. In order to separate hard photons from jets, a quark-to-photon fragmentation function á la Glover and Morgan is employed. Our results are implemented into Monte Carlo programs allowing for the evaluation of arbitrary differential cross sections. We present integrated cross sections for the LHC at 7 TeV, 8 TeV, and 14 TeV as well as differential distributions at 14 TeV for bare muons and dressed leptons. Finally, we discuss the impact of anomalous  $WW\gamma$  couplings.

# 1 Introduction

Lacking evidence for new physics at the LHC so far, precise investigations of Standard Model (SM) processes are more important than ever. While scrutinising the properties of the Higgs boson is the most pressing task, a continued detailed investigation of the electroweak (EW) gauge bosons has to be pursued as well. Besides single gauge-boson production in Drell–Yan processes, gauge-boson-pair production offers various ways of testing the gauge-boson sector of the SM thoroughly. One of the simplest gauge-boson-pair production processes is the production of a W boson in association with a photon,

$$pp \rightarrow W + \gamma + X \rightarrow l^+ \nu_l + \gamma + X. \quad (1.1)$$

Including the branching ratio for the leptonic W decay, it has a cross section in the picobarn range and allows for direct tests of the photon coupling to W bosons. Moreover, it constitutes a primary background to new-physics searches. Like other di-boson production processes,  $W\gamma$  production has already been measured at the Tevatron [1,2] and at the LHC [3–6], with experimental accuracies of roughly 12% on integrated cross sections. Up to now, no significant discrepancy between SM predictions and measurements is seen, a statement that translates into constraints on anomalous  $WW\gamma$  couplings at the level of  $\sim 0.3$  and  $\sim 0.04$  for the coupling parameters  $\Delta\kappa_\gamma$  and  $\lambda_\gamma$ , respectively. Since the sensitivity to anomalous couplings increases with the reach in the high-energy tails of distributions, even tighter constraints are expected from run 2 of the LHC close to its design energy of 14 TeV with higher luminosity. Especially the increasing precision of upcoming LHC results asks for higher precision in predictions.

The leading-order (LO) cross section for  $W\gamma$  production with on-shell (stable) W bosons was published 35 years ago [7]. The corresponding next-to-leading-order (NLO) QCD corrections for on-shell W bosons were calculated in Refs. [8,9] and extended to include leptonic decays in the narrow-width approximation and anomalous couplings in Ref. [10]. Based on full NLO QCD amplitudes including leptonic decays [11], a Monte Carlo program was presented for  $W\gamma$  production in Ref. [12], treating the leptonic decays of the W boson in the narrow-width approximation, but retaining all spin information via decay-angle correlations. In this approximation NLO QCD predictions are, for instance, available in the public program MCFM [13]. The QCD corrections enhance the cross section for  $W\gamma$  production at the LHC considerably and thus have a large impact on the measurement of the  $WW\gamma$  coupling. While gluon-induced NNLO corrections to  $W\gamma$  production including anomalous couplings were calculated in Ref. [14], recently first results of a complete NNLO calculation have been published [15]. NLO QCD corrections have been interfaced to QCD+QED parton showers using the POWHEG+MiNLO method [16].

It is known since many years that EW corrections can have a sizeable impact at high energies owing to the presence of logarithmically enhanced contributions [17–21]. In particular, distributions of energy-dependent observables may be affected at the level of several 10%. The logarithmically enhanced EW corrections for  $W\gamma$  production were discussed in Ref. [22] and shown to be negative at the level of 5–20%. The full EW corrections to  $W\gamma$  production including W-boson decays in the pole approximation were presented in Ref. [23].

In this paper we extend the existing calculations for  $W\gamma$  production in several respects arriving at a complete NLO QCD+EW calculation for  $pp \rightarrow l^+ \nu_l \gamma + X$ . To this end, we include the complete EW one-loop corrections to the partonic processes  $q_i \bar{q}_j \rightarrow l^+ \nu_l \gamma$ , i.e. we take all off-shell effects of the W boson into account. Moreover, we include the photon-induced partonic processes  $q_i \gamma \rightarrow l^+ \nu_l \gamma q_j$ ,  $\bar{q}_i \gamma \rightarrow l^+ \nu_l \gamma \bar{q}_j$ . Like in the calculation of QCD corrections, this requires to separate hard photons from jets. In order to define this separation in an infrared-safe way, we use a quark-to-photon fragmentation function [24,25].

This paper is organized as follows: In Section 2 we give the details of the calculation, including the general setup and the methods used for the virtual and real corrections. Our numerical results for total cross sections and distributions in various setups as well as with anomalous couplings are presented in Section 3, while Section 4 contains our conclusions.

## 2 Details of the calculation

### 2.1 General setup

The production of a leptonically decaying  $W^+$  boson in combination with a photon is ruled by quark–antiquark annihilation at LO,

$$u_i \bar{d}_j \rightarrow l^+ \nu_l \gamma, \quad (2.1)$$

where  $u_i$  and  $\bar{d}_j$  indicate the up-type quarks and the down-type antiquarks of the first two generations ( $i, j = 1, 2$ ). The charged lepton and the corresponding neutrino are denoted by  $l$  and  $\nu_l$ , where  $l = e, \mu$ . The LO Feynman diagrams for process (2.1) are shown in Fig. 1. In this work we present NLO corrections to  $W^+ + \gamma$  production which can be divided in EW and QCD corrections of the order  $\mathcal{O}(\alpha)$  and  $\mathcal{O}(\alpha_s)$ , respectively.

We denote the LO cross section calculated with LO parton distribution functions (PDFs) by  $\sigma^{\text{LO}}$ . The NLO-QCD-corrected cross section is obtained as

$$\begin{aligned} \sigma^{\text{NLO QCD}} &= \sigma^0 + \Delta\sigma^{\text{NLO QCD}}, \\ \Delta\sigma^{\text{NLO QCD}} &= \sigma_{\text{real}}^{\alpha_s} + \sigma_{\text{virt}}^{\alpha_s} + \sigma_{\text{col}}^{\alpha_s} + \sigma_{\text{frag}}^{\alpha_s}, \end{aligned} \quad (2.2)$$

where all contributions, including the LO cross section  $\sigma^0$ , are calculated with NLO PDFs. The real and the virtual corrections are given by  $\sigma_{\text{real}}^{\alpha_s}$  and  $\sigma_{\text{virt}}^{\alpha_s}$ , respectively, the contribution  $\sigma_{\text{col}}^{\alpha_s}$  originates from the redefinition of the PDFs, and  $\sigma_{\text{frag}}^{\alpha_s}$  represents the contribution from fragmentation of a quark into a photon. All individual parts in the NLO QCD contribution  $\Delta\sigma^{\text{NLO QCD}}$  are infrared (IR) divergent and only their sum is IR finite. While the separation between  $W + \gamma$  and  $W + \text{jet}$  production is evident at LO, the final states  $l^+ \nu_l \gamma g$ ,  $l^+ \nu_l \gamma d_j$ , and  $l^+ \nu_l \gamma \bar{u}_i$  appearing in the real NLO corrections to both  $W + \gamma$  and  $W + \text{jet}$  production require special care. The technical details of this aspect are discussed in Section 2.3.3.

Analogously to the QCD corrections, the EW corrections are given by

$$\begin{aligned} \Delta\sigma_{q\bar{q}}^{\text{NLO EW}} &= \sigma_{q\bar{q},\text{real}}^{\alpha} + \sigma_{q\bar{q},\text{virt}}^{\alpha} + \sigma_{q\bar{q},\text{col}}^{\alpha}, \\ \Delta\sigma_{q\gamma}^{\text{NLO EW}} &= \sigma_{q\gamma,\text{real}}^{\alpha} + \sigma_{q\gamma,\text{col}}^{\alpha} + \sigma_{q\gamma,\text{frag}}^{\alpha}, \end{aligned} \quad (2.3)$$

where the quark–antiquark-induced EW corrections  $\Delta\sigma_{q\bar{q}}^{\text{NLO EW}}$  and the photon-induced corrections  $\Delta\sigma_{q\gamma}^{\text{NLO EW}}$  are finite, while their individual contributions are IR divergent. Unlike the

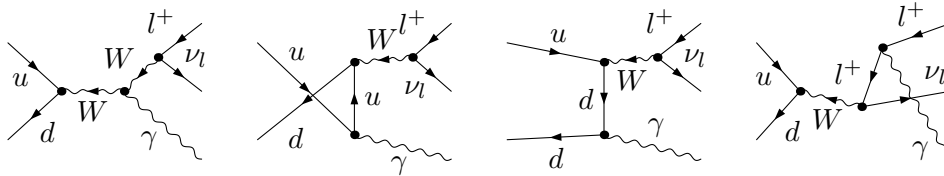


Figure 1: LO Feynman diagrams for the partonic process  $u_i \bar{d}_j \rightarrow l^+ \nu_l \gamma$ .

quark–antiquark- and the quark–gluon-induced channels in the QCD corrections,  $\Delta\sigma_{q\bar{q}}^{\text{NLO EW}}$  and  $\Delta\sigma_{q\gamma}^{\text{NLO EW}}$  can (in principle) be distinguished by their final states. Analogously to the QCD case,  $\sigma_{ij,\text{real}}^\alpha$  and  $\sigma_{q\bar{q},\text{virt}}^\alpha$  denote the real and the virtual corrections, respectively, and  $ij = q\bar{q}, q\gamma$ . Terms originating from the PDF redefinition furnish  $\sigma_{ij,\text{col}}^\alpha$ , and the fragmentation contribution is described by  $\sigma_{q\gamma,\text{frag}}^\alpha$ . Note that no fragmentation contribution is required in the  $q\bar{q}$  channel at NLO EW, because there is no jet in the final state in this order.

We choose to combine QCD and EW corrections using the naive product

$$\begin{aligned}\sigma^{\text{NLO}} &= \sigma^{\text{LO}} (1 + \delta_{\text{QCD}}) (1 + \delta_{\text{EW},q\bar{q}} + \delta_{\text{EW},q\gamma}) \\ &= \sigma^{\text{NLO QCD}} (1 + \delta_{\text{EW},q\bar{q}} + \delta_{\text{EW},q\gamma}),\end{aligned}\tag{2.4}$$

where the relative QCD, EW, and photon-induced corrections are defined by

$$\delta_{\text{QCD}} = \frac{\sigma^{\text{NLO QCD}} - \sigma^{\text{LO}}}{\sigma^{\text{LO}}}, \quad \delta_{\text{EW},q\bar{q}} = \frac{\Delta\sigma_{q\bar{q}}^{\text{NLO EW}}}{\sigma^0}, \quad \delta_{\text{EW},q\gamma} = \frac{\Delta\sigma_{q\gamma}^{\text{NLO EW}}}{\sigma^0},\tag{2.5}$$

respectively. While the relative QCD corrections are normalized to the LO cross section  $\sigma^{\text{LO}}$ , calculated with LO PDFs, the EW corrections are normalized to the LO cross section  $\sigma^0$ , calculated with NLO PDFs. By this definition,  $K_{\text{QCD}} = 1 + \delta_{\text{QCD}}$  is the standard QCD factor, and the relative EW corrections are practically independent of the PDF set.

In order to calculate the necessary amplitudes in the 't Hooft–Feynman gauge we use traditional methods based on Feynman diagrams. Two independent calculations were performed to guarantee the accuracy of the presented results. In both cases we employ the Weyl–van-der-Waerden spinor formalism as formulated in Ref. [26] for the numerical evaluation of the amplitudes. For the numerical calculation of the loop integrals the COLLIER library [27] is used, which is based on the results of Refs. [28–30] and involves two different independent implementations of all one-loop integrals.

One amplitude calculation is based on the program POLE [22], which internally uses FEYNARTS 3 [31, 32] and FORMCALC [33] for the generation of the amplitudes. The numerical integration is performed by the multi-channel phase-space generator LUSIFER [34] extended to use Vegas [35, 36] in order to optimize each phase-space mapping.

In the second calculation the virtual amplitudes are generated by FEYNARTS 1 [37] and algebraically reduced with an in-house MATHEMATICA package, automatically transferring the results into a FORTRAN code. For the numerical evaluation of integrated and differential cross sections the amplitudes are implemented into a FORTRAN program using the VEGAS algorithm for a proper numerical integration. In case of  $W + \gamma$  production sharp resonances appear, demanding additional phase-space mappings. Therefore, analytical Breit–Wigner mappings are introduced in the phase-space parametrization, allowing for a stable numerical integration by flattening the integrand.

## 2.2 Virtual corrections

In this section we shortly discuss the calculation of the virtual QCD and EW corrections to the partonic process (2.1). The QCD corrections receive contributions from self-energy, vertex, and box (4-point) diagrams only. The NLO EW corrections in addition involve pentagon (5-point) diagrams. The structural diagrams for the NLO EW corrections are shown in Figs. 2–5. There are about 280 EW one-loop diagrams involving 50 box and 16 pentagon diagrams (presented in Fig. 6).

For the proper description of the resonant W-boson propagators we use the complex-mass scheme [38–40]. In this scheme the W- and Z-boson masses are consistently treated as complex quantities, defined as the locations of the propagator poles in the complex plane. As a consequence the electroweak mixing angle and many couplings become complex as well. The complex-mass

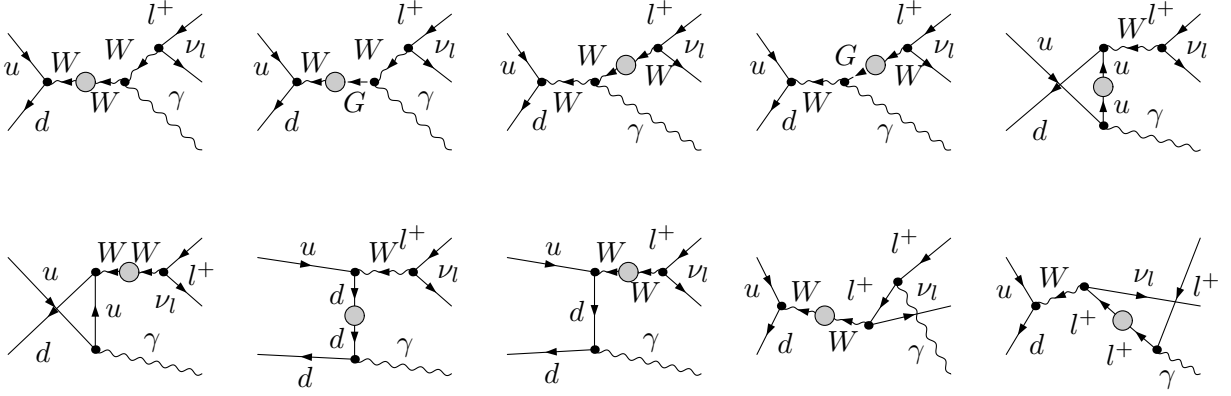


Figure 2: Self-energy corrections to the partonic process  $u_i \bar{d}_j \rightarrow l^+ \nu_l \gamma$ .

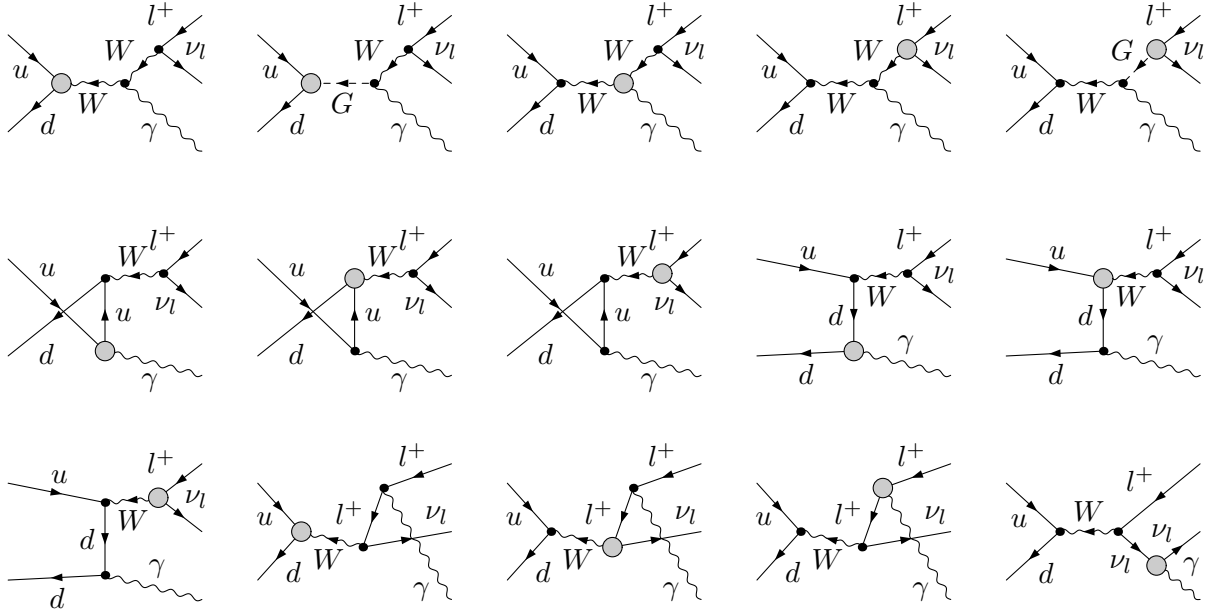


Figure 3: Vertex corrections to the partonic process  $u_i \bar{d}_j \rightarrow l^+ \nu_l \gamma$ .

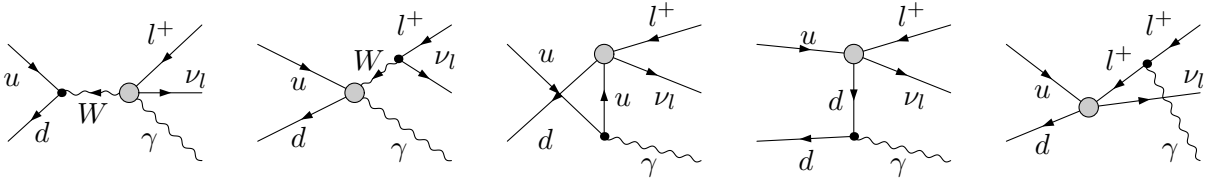


Figure 4: Box corrections to the partonic process  $u_i \bar{d}_j \rightarrow l^+ \nu_l \gamma$ .

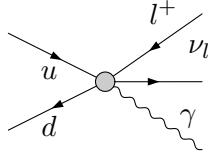


Figure 5: Pentagon corrections for the partonic process  $u_i \bar{d}_j \rightarrow l^+ \nu_l \gamma$ .

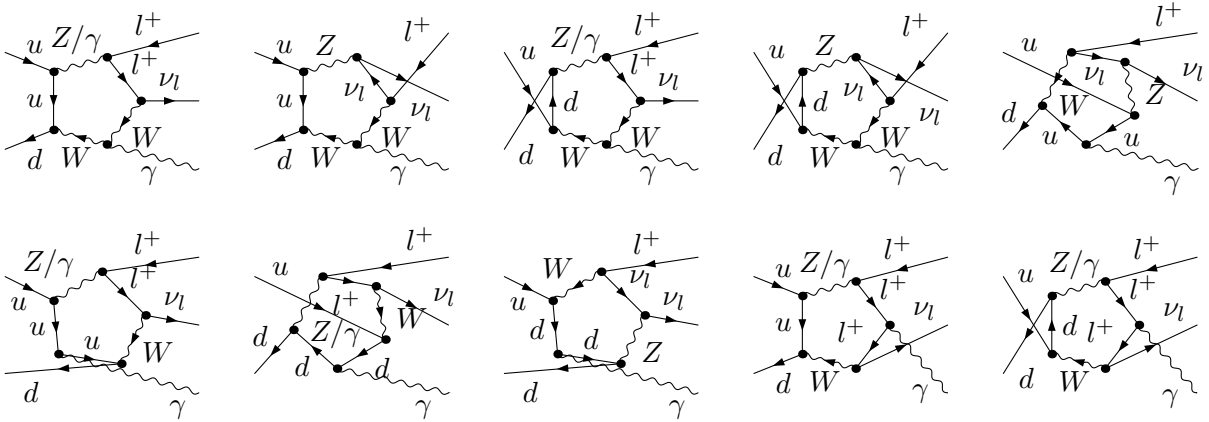


Figure 6: Explicit pentagon diagrams for the partonic process  $u_i \bar{d}_j \rightarrow l^+ \nu_l \gamma$ .

scheme fully respects gauge invariance, i.e. the underlying Ward identities are fulfilled and no dependence on the gauge-fixing procedure remains.

The one-loop amplitude can be represented in terms of standard matrix elements, which comprise all polarization-dependent quantities, and invariant coefficients, which are linear combinations of tensor-integral coefficients [41]. The tensor integral coefficients are evaluated with the library COLLIER [27]. The tensor integrals are recursively reduced to master integrals at the numerical level. All 5-point functions are directly reduced to 4-point functions based on the methods of Refs. [28, 29, 42]. The reduction to 4-point integrals uses the Passarino–Veltman algorithm [43] as well as dedicated expansion methods for exceptional phase-space regions [29]. The one-loop scalar integrals are evaluated with complex masses using the methods and results of Refs. [30, 44–46].

Ultraviolet divergences are regularized dimensionally. For IR singularities (soft and/or collinear) we either use pure dimensional regularization or alternatively pure mass regularization with infinitesimal gluon and photon masses and small fermion masses, which are only kept in the arguments of mass-singular logarithms. The results obtained with the two different IR regularizations are in perfect numerical agreement.

We use the on-shell renormalization as described in Ref. [39] for the complex-mass scheme. The strong coupling constant is renormalized in the  $\overline{\text{MS}}$  scheme with five active flavours with the top quark decoupled from the running of the strong coupling constant.

### 2.3 Real corrections

The real corrections are induced by the radiation of an additional photon or QCD parton. In order to isolate the soft and collinear divergences in the phase-space integration, the dipole subtraction formalism is applied. Specifically we use the QCD dipoles introduced in Refs. [47, 48] for the

calculation of the real QCD corrections and the QED dipoles introduced in Refs. [49, 50] for the evaluation of the real EW corrections. First we focus on the real EW corrections, where we distinguish between collinear-safe and non-collinear-safe observables. Then we discuss the quark-photon-induced channels and the real QCD corrections. As already mentioned, at NLO a simple separation of  $W + \gamma$  and  $W + \text{jet}$  production is not possible. Therefore, the concept of democratic clustering and the quark-to-photon fragmentation function are introduced, allowing for a well-defined separation of the two processes.

### 2.3.1 Real EW corrections

We first focus on the quark-antiquark-induced EW corrections where the final state contains two photons,

$$u_i \bar{d}_j \rightarrow l^+ \nu_l \gamma \gamma. \quad (2.6)$$

The corresponding Feynman diagrams are shown in Fig. 7. These contributions include soft and collinear singularities. While the soft singularities completely cancel against corresponding contributions in the virtual corrections, the cancellation of collinear singularities between real and virtual corrections is only partial in general. In the following we separately discuss the treatment of collinear singularities originating from photon radiation off initial-state (IS) or final-state (FS) leptons.

Following the standard treatment in the QCD-improved parton model, singularities connected to collinear splittings of IS partons are considered to be part of the incoming proton and are absorbed into the PDFs ( $f_q$ ) by the redefinition (see, e.g., Refs. [51, 52])

$$f_q(x) \rightarrow f_q(x, \mu_F^2) - \frac{\alpha}{2\pi} Q_q^2 \int_x^1 \frac{dz}{z} f_q\left(\frac{x}{z}, \mu_F^2\right) \times \left\{ \ln\left(\frac{\mu_F^2}{m_q^2}\right) [P_{ff}(z)]_+ - [P_{ff}(z)(2\ln(1-z) + 1)]_+ + C_{ff}(z) \right\}, \quad (2.7)$$

where  $x$  is the energy fraction carried by the parton coming from a proton,  $\mu_F$  is the factorization scale, and  $m_q$  and  $Q_q$  are the quark mass and charge, respectively. The splitting function is given by

$$P_{ff}(z) = \frac{1+z^2}{1-z}, \quad (2.8)$$

where  $[\dots]_+$  denotes the usual (+)-distribution prescription

$$\int_0^1 dx \left[ f(x) \right]_+ g(x) = \int_0^1 dx f(x) [g(x) - g(1)], \quad (2.9)$$

with  $g(x)$  representing a smooth test function.

The coefficient function  $C_{ff}$  defines the factorization scheme. Actually the  $\mathcal{O}(\alpha)$ -corrected NLO PDF set NNPDF23 [53] is only of LO with respect to QED corrections, i.e. they do not uniquely define a factorization scheme, but they should be most adequately used in a DIS-like factorization scheme for QED corrections (see Ref. [54] for arguments), so that the coefficient function reads

$$C_{ff}^{\text{DIS}}(z) = \left[ P_{ff}(z) \left( \ln\left(\frac{1-z}{z}\right) - \frac{3}{4} \right) + \frac{9+5z}{4} \right]_+. \quad (2.10)$$

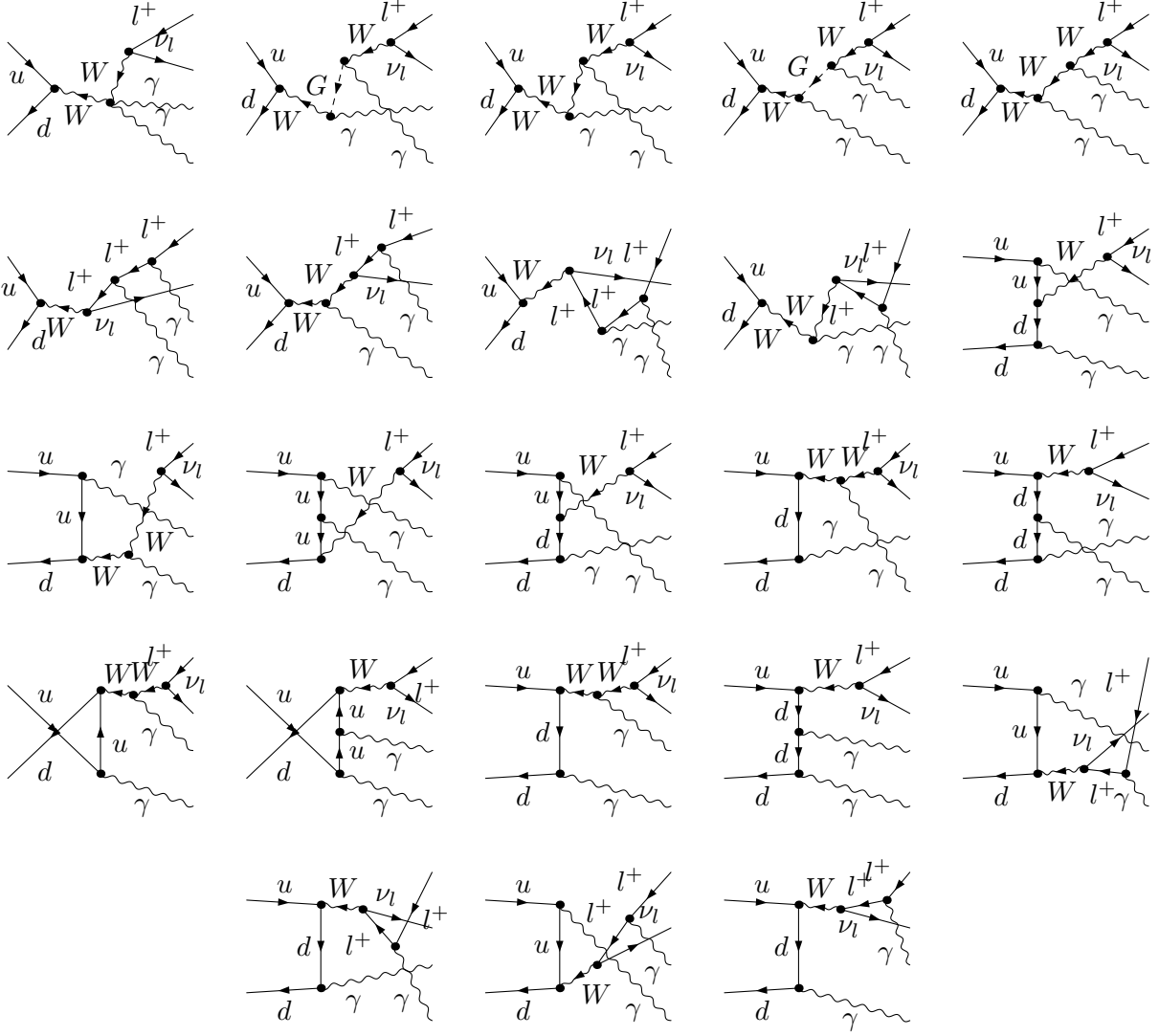


Figure 7: Feynman diagrams of the quark-antiquark-induced real EW corrections for the partonic process  $u_i \bar{d}_j \rightarrow l^+ \nu_l \gamma \gamma$ .

The cancellation of collinear singularities connected with photon emission of FS leptons depends on the level of inclusiveness in the event reconstruction. Trying to simulate the experimental setup as close as possible, two scenarios are considered. The first scenario is typical for a FS electron, which experimentally cannot be separated from a collinear photon. In the electromagnetic calorimeter only an electromagnetic shower is detected that is declared as a charged lepton. Technically this means that the charged lepton and the photon are recombined to one particle in the collinear regime, leading to a complete cancellation of the corresponding IR singularities, as dictated by the KLN theorem [55, 56]. Therefore this case is called the collinear-safe (CS) case. The second scenario applies to a FS muon, which is detected in the muon chamber, while a collinear photon is absorbed in the electromagnetic calorimeter. Thus, in the calculation we should not recombine the muon and the photon even if they are produced collinearly. This separation of the photon and the



“bare” muon has an important implication on the energy fraction

$$z_f = \frac{p_f^0}{p_f^0 + k_\gamma^0}, \quad (2.11)$$

of a charged fermion  $f$  produced together with a photon in a fixed collinear cone, where  $p_f^0$  and  $k_\gamma^0$  are the energies of the charged lepton and the photon, respectively. The absence of photon recombination in general disturbs the inclusive integration over  $z_f$  in observables, which, however, is required for the cancellation of collinear singularities between the real and the virtual corrections. In this case mass-singular contributions of the form  $\alpha \ln(m_f)$  remain, and this scenario is called the non-collinear-safe (NCS) case.

In contrast to the virtual corrections where the IR singularities appear as analytic expressions after performing the loop integrations, in the real corrections the IR singularities emerge from the phase-space integration of the FS particles, which is best done numerically. In order to analytically extract those singularities from the numerical integration to allow for an analytical cancellation, the dipole subtraction method is used. This technique was introduced in Ref. [49] for CS photon radiation and extended to the NCS case in Ref. [50]. We only give a short overview of the latter case, which covers the CS case as well.

To extract the IR singularities from the real corrections, a so-called subtraction function  $|\mathcal{M}_{\text{sub}}|^2$  is subtracted from the squared real-emission amplitude cancelling all IR singularities and allowing for a stable numerical integration. The subtraction function is constructed out of the squared Born-level matrix element  $|\mathcal{M}_0|^2$  and the dipole functions  $g_{ff'}^{(\text{sub})}$ ,

$$|\mathcal{M}_{\text{sub}}(\Phi_1)|^2 = - \sum_{f \neq f'} Q_f \sigma_f Q_{f'} \sigma_{f'} e^2 g_{ff'}^{(\text{sub})}(p_f, p_{f'}, k) \left| \mathcal{M}_0(\tilde{\Phi}_{0,ff'}) \right|^2, \quad (2.12)$$

where  $p_f$ ,  $p_{f'}$ , and  $k$  are the emitter, the spectator, and the photon momenta, respectively. The projection of the  $(N+1)$ -particle phase space  $\Phi_1$  to the  $N$ -particle phase space is denoted as  $\tilde{\Phi}_{0,ff'}$ . The charges of the emitter and the spectator are given by  $Q_f$  and  $Q_{f'}$ , respectively, and the sign factors  $\sigma_{f/f'}$  indicate the charge flows taking the values  $+1(-1)$  for incoming (outgoing) fermions or outgoing (incoming) antifermions. Adding the subtraction function back and integrating it over the one-particle phase space containing the IR singularity, the IR singularity can be cancelled against the corresponding singularity from the virtual corrections analytically. As already mentioned, mass-singular contributions remain in the NCS case, since we cut on the energy fraction  $z_f$  of the charged lepton inside the photon radiation cone by histogram binning or by applying event-selection cuts. In practice this means that the dependencies on  $z_f$  have to be made explicit during the whole subtraction procedure. For the application of event-selection cuts, the momenta that enter the LO matrix element inside the subtraction function have to be transferred to an  $(N+1)$ -particle phase space with photon emission by the assignment

$$p_f \rightarrow z_{ff'} \tilde{p}_f^{(ff')}, \quad k \rightarrow (1 - z_{ff'}) \tilde{p}_f^{(ff')}, \quad p_{f'} \rightarrow \tilde{p}_{f'}^{(ff')}, \quad (2.13)$$

which splits the momentum  $\tilde{p}_f^{(ff')}$  of the emitter fermion  $f$  into the momenta  $p_f$  and  $k$  of a collinear pair of a fermion and a photon, respectively. The energy fraction  $z_{ff'}$  defining this splitting tends to  $z_f$  of (2.11) in the corresponding singular limit. With this the subtraction proceeds as follows,

$$\int d\Phi_1 \left[ |\mathcal{M}_{\text{real}}|^2 \Theta_{\text{cut}}(p_f, k, p_{f'}, \{k_n\}) - \sum_{f \neq f'} |\mathcal{M}_{\text{sub},ff'}|^2 \Theta_{\text{cut}} \left( z_{ff'} \tilde{p}_f^{(ff')}, (1 - z_{ff'}) \tilde{p}_f^{(ff')}, \tilde{p}_{f'}^{(ff')}, \{\tilde{k}_n\} \right) \right], \quad (2.14)$$

where the sum runs over all emitter–spectator pairs  $f, f'$ . The momenta of the remaining particles are denoted by  $\{\tilde{k}_n\}$ . The cut function  $\Theta_{\text{cut}}$  acting on the  $(N+1)$ -particle phase space equals one if the configuration of final-state momenta passes the cuts, and zero otherwise.

Adding the subtraction function  $\int d\Phi_1 |\mathcal{M}_{\text{sub},ff'}(\Phi_1)|^2$  back and integrating out the divergent part analytically, the dependence on  $z_f$  has to be kept explicit. Comparing with the CS case this leads to additional terms including a  $(+)$ -distribution acting on  $z_f$  and in case of an IS spectator a double  $(+)$ -distribution  $[\dots]_+^{(x,y)}$  defined by

$$\int_0^1 dx \int_0^1 dy \left[ f(x, y) \right]_+^{(x,y)} g(x, y) = \int_0^1 dx f(x, y) [g(x, y) - g(1, y) - g(x, 1) + g(1, 1)], \quad (2.15)$$

where  $g(x, y)$  is a smooth test function. In the following we only discuss the case of an IS spectator, since it is the most complicated. More details as well as the treatment of the remaining emitter–spectator cases can be found in Ref. [50]. The NCS extension of the CS subtraction procedure is constructed in such a way that the  $z_f$ -dependent contributions are added in a straight-forward manner. These additional terms, which become zero in the CS case, include the mass singularity that remains due to the incomplete cancellation of IR divergences originating from the virtual corrections. The final equation for the integrated subtraction function with a FS emitter and an IS spectator reads

$$\begin{aligned} \int d\Phi_1 |\mathcal{M}_{\text{sub},ia}(\Phi_1)|^2 &= -\frac{\alpha}{2\pi} Q_i \sigma_i Q_a \sigma_a \int_0^1 dx \int d\tilde{\Phi}_{0,ia}(P_{ia}^2, x) \int_0^1 dz \\ &\times \Theta_{\text{cut}} \left( p_i = z\tilde{p}_i(x), k = (1-z)\tilde{p}_i(x), \{\tilde{k}_n(x)\} \right) \\ &\times \frac{1}{x} \left\{ G_{ia}^{(\text{sub})}(P_{ia}^2) \delta(1-x) \delta(1-z) + \left[ \mathcal{G}_{ia}^{(\text{sub})}(P_{ia}^2, x) \right]_+ \delta(1-z) \right. \\ &\quad \left. + \left[ \bar{\mathcal{G}}_{ia}^{(\text{sub})}(P_{ia}^2, z) \right]_+ \delta(1-x) + \left[ \bar{g}_{ia}^{(\text{sub})}(x, z) \right]_+^{(x,z)} \right\} \left| \mathcal{M}_0(\tilde{p}_i(x), \tilde{p}_a(x), \{\tilde{k}_n(x)\}) \right|^2, \quad (2.16) \end{aligned}$$

where the fine-structure constant is defined by  $\alpha = e^2/(4\pi)$  and the indices  $i$  and  $a$  indicate the FS emitter and the IS spectator, respectively. The original momentum of the IS spectator is re-scaled by  $x$  ( $\tilde{p}_i = xp_i$ ). Therefore,  $d\tilde{\Phi}_{0,ia}(P_{ia}^2, x)$ , which indicates the phase-space measure of the momenta  $\tilde{p}_i(x)$ ,  $\tilde{p}_a(x)$ , and  $\{\tilde{k}_n(x)\}$  before FS radiation, is  $x$  dependent. Due to the  $(+)$ -distribution in  $x$ , two sets of phase-space momenta,  $\tilde{\Phi}_{0,ia}(P_{ia}^2, x)$  and  $\tilde{\Phi}_{0,ia}(P_{ia}^2, 1)$  have to be generated per phase-space point. The invariant  $P_{ia}^2 = (p_i - p_a + k)^2 = (\tilde{p}_i - \tilde{p}_a)^2$  has to be evaluated with the momenta entering the corresponding LO matrix element  $|\mathcal{M}_0|^2$ . The function  $\Theta_{\text{cut}}$  represents the application of the phase-space cuts on the  $(N+1)$ -particle phase space, where the momenta  $p_i$  and  $k$  are reconstructed from the momentum  $\tilde{p}_i(x)$  as given in (2.13). While line 3 of (2.16) describes the  $z$ -independent contributions which also appear in the CS case, line 4 contains the additional  $z$ -dependent terms emerging in the NCS scenario. In the case of a FS emitter and an IS spectator the endpoint function  $G_{ia}^{(\text{sub})}(P_{ia}^2)$  and the distribution  $\mathcal{G}_{ia}^{(\text{sub})}(P_{ia}^2, x)$  in the limit of  $m_i \rightarrow 0$  are given by

$$\begin{aligned} G_{ia}^{(\text{sub})}(P_{ia}^2) &= \mathcal{L}(|P_{ia}^2|, m_i^2) - \frac{\pi^2}{2} + \frac{3}{2}, \\ \mathcal{G}_{ia}^{(\text{sub})}(P_{ia}^2, x) &= \frac{1}{1-x} \left[ 2 \ln \left( \frac{2-x}{1-x} - \frac{3}{2} \right) \right], \quad (2.17) \end{aligned}$$

with

$$\mathcal{L}(P^2, m^2) = \ln \left( \frac{m^2}{P^2} \right) \ln \left( \frac{m_\gamma^2}{P^2} \right) + \ln \left( \frac{m_\gamma^2}{P^2} \right) - \frac{1}{2} \ln^2 \left( \frac{m^2}{P^2} \right) + \frac{1}{2} \ln \left( \frac{m^2}{P^2} \right). \quad (2.18)$$

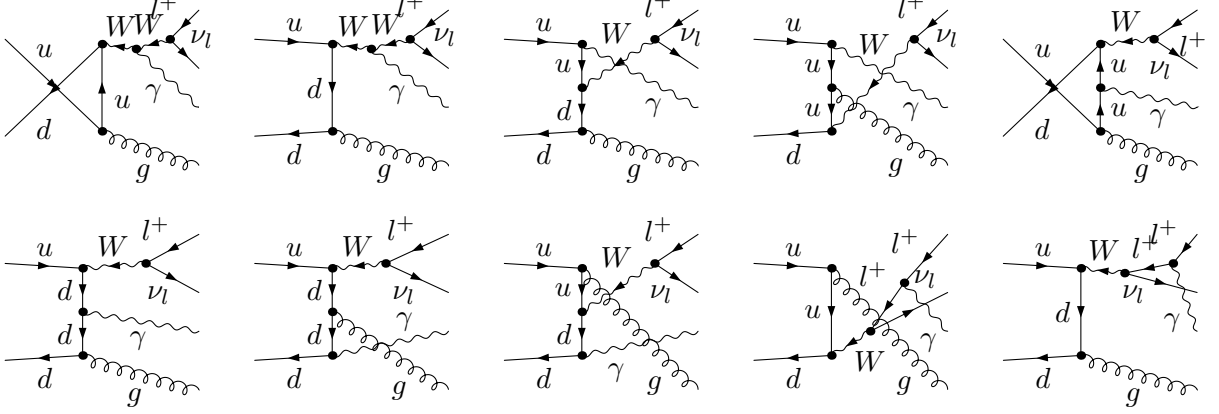


Figure 8: Feynman diagrams of the quark–antiquark-induced real QCD corrections for the partonic process  $u_i \bar{d}_j \rightarrow l^+ \nu_l \gamma g$ .

The functions containing the  $z$  dependence read

$$\begin{aligned} \bar{g}_{ia}^{(\text{sub})}(x, z) &= \frac{1}{1-x} \left( \frac{2}{2-x-z} - 1 - z \right), \\ \bar{\mathcal{G}}_{ia}^{(\text{sub})}(P_{ia}^2, z) &= P_{ff}(z) \left[ \ln \left( \frac{-P_{ia}^2 z}{m_i^2} \right) - 1 \right] - \frac{2 \ln(2-z)}{1-z} + (1+z) \ln(1-z) + (1-z), \end{aligned} \quad (2.19)$$

where the Altarelli–Parisi splitting function  $P_{ff}(z)$  is defined in (2.8). The remaining fermion-mass dependence originating from the incomplete cancellation of collinear singularities is included in the function  $\bar{\mathcal{G}}_{ia}^{(\text{sub})}(P_{ia}^2, z)$ .

### 2.3.2 Real QCD and photon-induced corrections

The real QCD and the real photon-induced corrections have the same FS signature and cause the same problem when a photon and a jet become collinear. Therefore, we discuss these corrections together. At NLO QCD the following channels contribute to the real corrections,

$$\begin{aligned} u_i \bar{d}_j &\rightarrow l^+ \nu_l \gamma g, \\ u_i g &\rightarrow l^+ \nu_l \gamma d_j, \\ \bar{d}_j g &\rightarrow l^+ \nu_l \gamma \bar{u}_i. \end{aligned} \quad (2.20)$$

The corresponding Feynman diagrams for the quark–antiquark-induced real corrections are shown in Fig. 8. The quark–gluon-induced channels can be obtained from the quark–antiquark-induced channel by crossing the gluon into the IS and the (anti)quark into the FS. For the extraction of the IR singularities from the real emission amplitudes the Catani–Seymour dipole-subtraction formalism is applied [47, 48].

Calculating the photon-induced corrections the following channels have to be taken into account,

$$\begin{aligned} u_i \gamma &\rightarrow l^+ \nu_l \gamma d_j, \\ \bar{d}_j \gamma &\rightarrow l^+ \nu_l \gamma \bar{u}_i. \end{aligned} \quad (2.21)$$

Collinear singularities from IS splittings are compensated by a redefinition of the PDFs (see, e.g., Ref. [52]),

$$f_q(x) \rightarrow f_q(x, \mu_F^2) - \frac{\alpha}{2\pi} 3Q_q^2 \int_x^1 \frac{dz}{z} f_\gamma\left(\frac{x}{z}, \mu_F^2\right) \left\{ \ln\left(\frac{\mu_F^2}{m_q^2}\right) P_{f\gamma}(z) + C_{f\gamma} \right\}, \quad (2.22)$$

where the splitting function is defined as

$$P_{f\gamma}(z) = z^2 + (1-z)^2, \quad (2.23)$$

and the factorization-scale-dependent coefficient function  $C_{f\gamma}(z)$  evaluated in the DIS scheme reads

$$C_{f\gamma}^{\text{DIS}}(z) = P_{f\gamma}(z) \ln\left(\frac{1-z}{z}\right) - 8z^2 + 8z - 1. \quad (2.24)$$

For extracting the collinear IS singularities from the real emission amplitude, the dipole subtraction formalism introduced in Ref. [50] is applied. Demanding a photon in the FS requires that the photon and the FS jet are separated in a well-defined way. This causes an additional complication that is discussed in the next section.

### 2.3.3 Quark-to-photon fragmentation function

At NLO we have to deal with photons that are radiated collinearly to a jet. Experimentally it is not possible to decide whether the photon comes from the hard scattering process or is generated during the hadronization of a quark or a gluon. Furthermore, a collinear divergence appears if the photon is radiated collinear to a FS quark. This divergence cancels if photons and QCD partons are treated on equal footing, i.e. if photon recombination with QCD partons is included in the jet algorithm. However, in such a procedure the two processes of  $W+\gamma$  and  $W+\text{jet}$  production are not separated at all, so that valuable experimental information would remain unexploited. To separate the two processes, a well-defined procedure is needed to differentiate between collinear photons and jets. Note that simply imposing a separation cut between the photon and the jet would spoil the cancellation of IR divergences.

The problem of separating the two processes can be solved by introducing the concept of democratic clustering and a quark-to-photon fragmentation function as suggested in Refs. [24, 25]. This concept treats photons and partons on equal footing, meaning that they are clustered to one photon-jet system if they are collinear. In this context the energy fraction of the photon inside the photon-jet system is defined as

$$z_\gamma = \frac{E_\gamma}{E_\gamma + E_{\text{jet}}}, \quad (2.25)$$

where  $E_\gamma$  and  $E_{\text{jet}}$  are the energies of the photon and the jet in the collinear regime, respectively. We define the photon-jet system as a photon if  $z_\gamma$  is larger than a certain cut value  $z_{\text{cut}}$ , otherwise we consider it as a jet and discard the event. The complementary approach was used in Ref. [57] to define  $W+\text{jet}$  production including NLO QCD+EW corrections; there events were only kept if  $z_\gamma$  was smaller than some value  $z_{\text{cut}}$ .

Based on this procedure a quark-to-photon fragmentation function has been measured by ALEPH [58]. This fragmentation function is used to compensate the collinear singularity (appearing if the quark radiates a collinear photon) by a redefinition of the fragmentation function similarly to the redefinition of the PDFs. At NNLO  $\mathcal{O}(\alpha_s^2)$  one would even have to introduce a gluon-to-photon fragmentation function.

For extracting the collinear singularity from the real corrections the QED dipole subtraction formalism from Ref. [50] is applied again. Following this method the subtraction function has the same structure as the subtraction function for the quark–antiquark-induced real EW corrections (2.12):

$$|\mathcal{M}_{\text{sub}}(\Phi_1)|^2 = - \sum_{\substack{f, f' \\ f \neq f'}} Q_f \sigma_f Q_{f'} \sigma_{f'} e^2 g_{ff'}^{(\text{sub})}(p_f, p_{f'}, k) \left| \mathcal{M}_0 \left( \tilde{\Phi}_{0, ff'} \right) \right|^2, \quad (2.26)$$

where  $\mathcal{M}_0$  is the Born matrix element of the process without photon radiation. Actually the sum over the emitter  $f$  runs over all charged fermions in the IS or FS of the process. However, demanding a resolved hard photon with non-vanishing  $p_T$  and separated from the FS lepton, effectively reduces this sum to the term where  $f$  is a FS quark or antiquark  $i$  appearing in the real NLO corrections. Photons collinear to IS partons are excluded by the photon acceptance cuts, photons collinear to FS leptons are excluded by dedicated separation cuts. The subtraction function, thus, reads

$$|\mathcal{M}_{\text{sub}}(\Phi_1)|^2 = - \sum_{f' \neq i} Q_i \sigma_i Q_{f'} \sigma_{f'} e^2 g_{if'}^{(\text{sub})}(p_i, p_{f'}, k) \left| \mathcal{M}_0^{\text{W+jet}} \left( \tilde{\Phi}_{0, if'} \right) \right|^2, \quad (2.27)$$

where  $i$  denotes an (anti-)up- or down-type quark and the matrix element  $\mathcal{M}_0^{\text{W+jet}}$  in (2.28) is the Born amplitude for W+jet production without a photon in the final state. Note also that identifying a collinear photon–jet pair as a photon only if  $z_\gamma > z_{\text{cut}}$  excludes the soft-photon singularity from the phase space relevant for  $W + \gamma$  production, i.e. only the collinear asymptotics of the dipole functions is required to obtain finite integrals. Since no soft singularity needs to be subtracted and all dipoles have the same collinear limit, they can be set equal (up to their charge factors), i.e. one specific emitter–spectator pair can be chosen. Furthermore, charge conservation can be used to eliminate the remaining sum  $\sum_{f' \neq i} \sigma_{f'} Q_{f'} = -\sigma_i Q_i$ . Choosing the charged FS lepton  $l$  as the spectator the subtraction function reads

$$|\mathcal{M}_{\text{sub}}(\Phi_1)|^2 = Q_i^2 e^2 g_{il}^{(\text{sub})}(p_i, p_l, k) \left| \mathcal{M}_0^{\text{W+jet}} \left( \tilde{p}_i, \tilde{p}_l, \{\tilde{k}_n\} \right) \right|^2. \quad (2.28)$$

The quantities  $\tilde{p}_i, \tilde{p}_l$ , and  $\{\tilde{k}_n\}$  represent the momenta of the projected phase space  $\tilde{\Phi}_0$ . Since in our case only a FS spectator appears, no boost has to be applied and the momenta  $\{\tilde{k}_n\}$  equal the momenta  $\{k_n\}$  of the  $(N + 1)$ -particle phase space. The W + jet Born processes are

$$\begin{aligned} u_i g &\rightarrow l^+ \nu_l d_j, \\ \bar{d}_j g &\rightarrow l^+ \nu_l \bar{u}_i \end{aligned} \quad (2.29)$$

with an IS gluon and

$$\begin{aligned} u_i \gamma &\rightarrow l^+ \nu_l d_j, \\ \bar{d}_j \gamma &\rightarrow l^+ \nu_l \bar{u}_i \end{aligned} \quad (2.30)$$

with an IS photon. The dipole subtraction function for the case of massless FS emitter and FS spectator from (2.28) is given by

$$g_{il}^{(\text{sub})} = \frac{1}{(p_i k)(1 - y_{il})} \left[ \frac{2}{1 - z_{il}(1 - y_{il})} - 1 - z_{il} \right], \quad (2.31)$$

where  $y_{il}$  and  $z_{il}$  are defined as follows,

$$y_{il} = \frac{p_i k}{p_i p_l + p_i k + p_l k}, \quad z_{il} = \frac{p_i p_l}{p_i p_l + p_l k} = 1 - z_{\gamma l}. \quad (2.32)$$

In the collinear limit  $(p_i k) \rightarrow 0$  they behave as  $y_{il} \rightarrow 0$ ,  $z_{il} \rightarrow z_i$ , and  $z_{\gamma l} \rightarrow z_\gamma$ , where  $z_i$  and  $z_\gamma$  are the energy fractions in the quark–photon system in the collinear limit,

$$z_i = \frac{E_i}{E_i + E_\gamma} = 1 - z_\gamma. \quad (2.33)$$

Otherwise, the subtraction procedure works analogously as for the real EW corrections in the NCS case,

$$\int d\Phi_1 \left[ |\mathcal{M}_{\text{real}}|^2 \Theta_{\text{cut}}(p_i, k, p_l, \{k_n\}) - |\mathcal{M}_{\text{sub}}|^2 \Theta_{\text{cut}}\left((1 - z_{\gamma l})\tilde{p}_i, z_{\gamma l}\tilde{p}_i, \tilde{p}_l, \{\tilde{k}_n\}\right) \right], \quad (2.34)$$

with the only difference that we make the dependence on  $z_{\gamma l}$  explicit instead of  $z_{il}$ , since we want to cut on  $z_{\gamma l}$ . Following the calculations in Refs. [50, 59], we find for the integrated dipole contribution to the partonic cross section

$$\begin{aligned} d\hat{\sigma}_{\text{sub}}(z_{\text{cut}}, m_i) &= \frac{\alpha Q_i^2}{4\pi \hat{s}} d\tilde{\Phi}_0 \int_{z_{\text{cut}}}^1 dz_\gamma \bar{\mathcal{G}}_{il}^{(\text{sub})}(P_{il}^2, 1 - z_\gamma) \\ &\times \left| \mathcal{M}_0^{W+\text{jet}}(\tilde{p}_i, \tilde{p}_l, \{\tilde{k}_n\}) \right|^2 \Theta_{\text{cut}}\left(p_i = (1 - z_\gamma)\tilde{p}_i, k = z_\gamma\tilde{p}_i, \tilde{p}_l, \{\tilde{k}_n\}\right), \end{aligned} \quad (2.35)$$

where  $z_{\text{cut}}$  is the lower limit on  $z_\gamma$  and  $\sqrt{\hat{s}}$  is the centre-of-mass energy of the partonic scattering process. Note that the soft-singular endpoint appearing at  $z_\gamma \rightarrow 0$  is excluded by the cut  $z_\gamma > z_{\text{cut}}$ , so that we need not introduce a plus distribution to isolate a soft singularity. The function  $\bar{\mathcal{G}}^{(\text{sub})}$  for FS emitter and FS spectator reads

$$\bar{\mathcal{G}}_{il}^{(\text{sub})}(P_{il}^2, z_i) = P_{ff}(z_i) \left[ \ln\left(\frac{P_{il}^2 z_i}{m_i^2}\right) - 1 \right] + (1 - z_i) \ln(1 - z_i) + (1 - z_i), \quad (2.36)$$

where  $P_{il}^2$  is the squared invariant mass of the FS quark and the charged lepton, and  $m_i$  is the quark mass regularizing the collinear singularity.

The subtraction procedure outlined above does not remove the FS singularity appearing in collinear photon–jet pairs, it only isolates the corresponding divergence in terms of a logarithm  $\ln m_i$  of the light-quark mass  $m_i$  (or alternatively a dimensionally regularized divergence). In order to restore IR safety the situation where a FS quark fragments into a collinear quark–photon pair has to be considered. The occurring mass singularity can be treated by introducing a quark-to-photon fragmentation function  $D_{q \rightarrow \gamma}(z_\gamma)$  which is defined in Refs. [24, 25] and was measured in Ref. [58]. It describes the probability that a quark fragments into a photon with the energy fraction  $z_\gamma$ . As worked out in Ref. [25], the fragmentation contribution  $\hat{\sigma}_{\text{frag}}(z_{\text{cut}})$  to the partonic cross section is given by

$$d\hat{\sigma}_{\text{frag}}(z_{\text{cut}}) = d\hat{\sigma}_0 \int_{z_{\text{cut}}}^1 dz_\gamma D_{q \rightarrow \gamma}^{\text{bare}}(z_\gamma), \quad (2.37)$$

where  $d\hat{\sigma}_0$  denotes the partonic LO cross section. The collinear singularity can now be compensated by a redefinition of the bare fragmentation function  $D_{q \rightarrow \gamma}^{\text{bare}}$ . We split off the singular contribution regularized by the infinitesimal quark mass  $m_i$ , which introduces a dependence on the factorization scale  $\mu_F$  separating the perturbative from the non-perturbative region [59],

$$D_{q \rightarrow \gamma}^{\text{bare,MR}}(z_\gamma) = \frac{\alpha Q_i^2}{2\pi} P_{ff}(1 - z_\gamma) \left( \ln \frac{m_i^2}{\mu_F^2} + 2 \ln z_\gamma + 1 \right) + D_{q \rightarrow \gamma}^{\text{MS}}(z_\gamma, \mu_F), \quad (2.38)$$

where the label “MR” stands for the employed mass regularization. As shown in Ref. [59], the finite contribution  $D_{q \rightarrow \gamma}^{\overline{\text{MS}}}$  defined in this way is equivalent to the standard  $\overline{\text{MS}}$  scheme of dimensional regularization. Here, we employ the parametrization used by the ALEPH collaboration [58]

$$D_{q \rightarrow \gamma}^{\text{ALEPH}, \overline{\text{MS}}}(z_\gamma, \mu_F) = \frac{\alpha Q_i^2}{2\pi} \left( P_{ff}(1 - z_\gamma) \ln \frac{\mu_F^2}{(1 - z_\gamma)^2 \mu_0^2} + C \right). \quad (2.39)$$

The fit parameters  $\mu_0^2$  and  $C$  constrained by  $C = -1 + \ln(2\mu_0^2/M_Z^2)$  are

$$\mu_0 = 0.14 \text{ GeV} \text{ and } C = -13.26. \quad (2.40)$$

Combining (2.35) and (2.38), setting  $1 - z_\gamma = z_i$  and performing the  $z_i$ -integration analytically leads to (see Eq. (4.63) in Ref. [59])

$$\begin{aligned} & d\hat{\sigma}_{\text{sub}}(z_{\text{cut}}, m_i) + d\hat{\sigma}_{\text{frag}}(z_{\text{cut}}, m_i) \\ &= \frac{\alpha Q_i^2}{4\pi \hat{s}} d\tilde{\Phi}_0 \left| \mathcal{M}_0^{W+\text{jet}}(\tilde{\Phi}_0) \right|^2 \int_0^{1-z_{\text{cut}}} dz_i \left( D_{q \rightarrow \gamma}^{\text{bare, MR}}(1 - z_i) + \bar{\mathcal{G}}_{il}^{(\text{sub})}(P_{il}^2, z_i) \right) \\ &= \frac{\alpha Q_i^2}{4\pi \hat{s}} d\tilde{\Phi}_0 \left| \mathcal{M}_0^{W+\text{jet}}(\tilde{\Phi}_0) \right|^2 \left\{ \left( 1 + C + \frac{z_{\text{cut}}}{2} \right) (1 - z_{\text{cut}}) \right. \\ &\quad \left. - \left( \frac{1}{2}(1 - z_{\text{cut}})(3 - z_{\text{cut}}) + 2 \ln(z_{\text{cut}}) \right) \ln \left( \frac{z_{\text{cut}}}{1 - z_{\text{cut}}} \frac{P_{il}^2}{\mu_0^2} \right) \right. \\ &\quad \left. + 2 \text{Li}_2(1 - z_{\text{cut}}) + \frac{3}{2} \ln(z_{\text{cut}}) \right\}, \end{aligned} \quad (2.41)$$

which is finite and only depends on the value  $z_{\text{cut}}$ .

### 3 Numerical results

#### 3.1 Input parameters and setup

The relevant SM input parameters are

$$\begin{aligned} G_\mu &= 1.1663787 \times 10^{-5} \text{ GeV}^{-2}, & \alpha(0) &= 1/137.035999074, & \alpha_s(M_Z) &= 0.119, \\ M_H &= 125 \text{ GeV}, & m_\mu &= 105.6583715 \text{ MeV}, & m_t &= 173.07 \text{ GeV}, \\ M_W^{\text{OS}} &= 80.385 \text{ GeV}, & \Gamma_W^{\text{OS}} &= 2.085 \text{ GeV}, \\ M_Z^{\text{OS}} &= 91.1876 \text{ GeV}, & \Gamma_Z^{\text{OS}} &= 2.4952 \text{ GeV}, \\ |V_{us}| &= |V_{cd}| = 0.225, & |V_{ud}| &= |V_{cs}| = \sqrt{1 - |V_{us}|^2}. \end{aligned} \quad (3.1)$$

All parameters but  $\alpha_s(M_Z)$ , which is provided by the PDF set, are extracted from Ref. [60]. The masses of all quarks but the top quark are set to zero. CKM mixing between the first two quark generations is taken into account in all partonic cross sections, but mixing to the third generation is not included, since it is negligible. This implies that there is no contribution from bottom quarks in the initial state and that the CKM matrix drops out in the flavour sum of closed fermion loops. Thus, the CKM matrix factorizes from all amplitudes, so that only one generic amplitude has to be evaluated when convoluting the squared matrix elements with the PDFs.

Owing to the presence of an on-shell external photon, we always take one electromagnetic coupling constant  $\alpha$  at zero momentum transfer,  $\alpha = \alpha(0)$ . For the other couplings, e.g. of the

W boson to fermions, we determine the electromagnetic coupling constant in the  $G_\mu$  scheme, where  $\alpha$  is defined in terms of the Fermi constant,

$$\alpha_{G_\mu} = \frac{\sqrt{2}}{\pi} G_\mu M_W^2 \left( 1 - \frac{M_W^2}{M_Z^2} \right). \quad (3.2)$$

This definition effectively resums contributions associated with the evolution of  $\alpha$  from zero momentum transfer to the electroweak scale and includes universal corrections to the  $\rho$ -parameter. In this scheme large fermion-mass logarithms are effectively resummed leading to an independence of logarithms of the light fermion masses [39] (see also the discussion in the “EW dictionary” in Ref. [61]). Using this mixed scheme the squared LO amplitude is proportional to  $\alpha(0)\alpha_{G_\mu}^2$ . In the relative EW corrections we set the additional coupling factor  $\alpha$  to  $\alpha_{G_\mu}$ , because this coupling is adequate for the most pronounced EW corrections which are caused by soft/collinear weak gauge-boson exchange at high energies (EW Sudakov logarithms, etc.).

We apply the complex-mass scheme [38–40] to describe the W-boson resonance by introducing complex vector-boson masses according to

$$M_W^2 \rightarrow \mu_W^2 = M_W^2 - iM_W\Gamma_W, \quad M_Z^2 \rightarrow \mu_Z^2 = M_Z^2 - iM_Z\Gamma_Z \quad (3.3)$$

with constant widths. However, at LEP and the Tevatron the on-shell (OS) masses of the vector bosons were measured, which correspond to running widths. The OS masses  $M_W^{\text{OS}}$ ,  $M_Z^{\text{OS}}$  and widths  $\Gamma_W^{\text{OS}}$ ,  $\Gamma_Z^{\text{OS}}$  have to be converted to the pole values using the relations [62]

$$M_V = M_V^{\text{OS}} / \sqrt{1 + (\Gamma_V^{\text{OS}}/M_V^{\text{OS}})^2}, \quad \Gamma_V = \Gamma_V^{\text{OS}} / \sqrt{1 + (\Gamma_V^{\text{OS}}/M_V^{\text{OS}})^2} \quad (V = W, Z), \quad (3.4)$$

leading to

$$\begin{aligned} M_W &= 80.3580 \dots \text{ GeV}, & \Gamma_W &= 2.0843 \dots \text{ GeV}, \\ M_Z &= 91.1535 \dots \text{ GeV}, & \Gamma_Z &= 2.4943 \dots \text{ GeV}. \end{aligned} \quad (3.5)$$

Calculating the hadronic cross section, we use the  $\mathcal{O}(\alpha)$ -corrected NLO PDF set NNPDF23 [53], which includes the two-loop running of  $\alpha_s$  for five active flavours ( $n_f = 5$ ).

The factorization and the renormalization scales  $\mu_F, \mu_R$  are set equal throughout our calculation. Following Refs. [63, 64], we choose the scales as

$$\mu_F^2 = \mu_R^2 = \frac{1}{2} \left( M_W^2 + p_{T,W}^2 + p_{T,\gamma_1}^2 + p_{T,\gamma_2/\text{jet}}^2 \right), \quad (3.6)$$

where  $p_{T,W}$  is the transverse momentum of the massive vector boson defined by

$$p_{T,W} = |\mathbf{p}_{T,l} + \mathbf{p}_{T,\nu}|, \quad (3.7)$$

and  $p_{T,a} = |\mathbf{p}_{T,a}|$  denotes the absolute value of the transverse three-momentum  $\mathbf{p}_{T,a}$  of particle  $a$ . The photons  $\gamma_1$  and  $\gamma_2$  are assigned so that  $p_{T,\gamma_1} > p_{T,\gamma_2}$ . In LO the transverse momenta  $p_{T,\gamma_2/\text{jet}}$  are zero.

### 3.2 Phase-space cuts and event selection

The process  $pp \rightarrow W^+ + \gamma \rightarrow l^+ \nu_l + \gamma + X$  requires the recombination of FS photons with FS partons and, where appropriate, of FS photons with charged leptons in regimes of phase space where photon and parton/lepton are collinear. Furthermore, we impose several cuts to account for the detector acceptance. The phase-space cuts and the event selection are inspired by the recent ATLAS and CMS papers [3–5] analysing  $V\gamma$  final states.



### 3.2.1 Recombination

To decide whether a photon and a FS particle need to be recombined we use the Euclidean distance in the  $y$ - $\phi$  plane,  $R_{ij} = \sqrt{(y_i - y_j)^2 + \phi_{ij}^2}$ , where  $y = \frac{1}{2} \ln [(E + p_L) / (E - p_L)]$  denotes the rapidity. In this equation  $E$  is the energy and  $p_L$  the longitudinal momentum of the respective particle with respect to the beam axis. The value  $\phi_{ij}$  denotes the angle between the particles  $i$  and  $j$  in the plane perpendicular to the beams. The recombination proceeds as follows:

1. A photon and a charged lepton are never recombined if we consider “bare” muons. Otherwise recombination is applied if  $R_{l+\gamma} < 0.1$ , which means that their four-momenta are added. In case of two photons in the final state, the recombination is first done with the photon that yields the smaller  $R_{l+\gamma}$ , then this condition is checked for the second photon.
2. Two photons are recombined if  $R_{\gamma\gamma} < 0.1$ .
3. A photon and a jet are recombined if the distance between them becomes  $R_{\gamma\text{jet}} < 0.5$ . After recombining them, the energy fraction  $z_\gamma = E_\gamma / (E_\gamma + E_{\text{jet}})$  of the photon inside the photon–jet system is determined. If  $z_\gamma$  is smaller than the cut value  $z_{\text{cut}} = 0.9$  the event is regarded as a part of the process  $W + \text{jet}$  and is therefore rejected.

The case where more than two particles are recombined is excluded by our basic cuts. Results are presented for “bare” muons and for photon recombination with leptons. The latter results hold for electrons as well as for muons, since the lepton-mass logarithms cancel as dictated by the KLN theorem [55, 56].

### 3.2.2 Basic cuts

After recombination, we define  $W + \gamma$  events by the following cut procedure:

1. We demand a charged lepton with transverse momentum  $p_{T,l} > 25$  GeV and missing transverse momentum  $\cancel{p}_T > 25$  GeV, where  $\cancel{p}_T$  is equal to the neutrino transverse momentum.
2. We demand at least one photon with transverse momentum  $p_{T,\gamma} > 15$  GeV that is isolated from the charged lepton with a distance of  $R_{l+\gamma} > 0.7$ .
3. The charged lepton and the photon passing the cuts at step 2 have to be central, i.e. their rapidities have to be in the range  $|y| < 2.5$ .
4. Only events with a transverse mass of the lepton pair  $M_{T,l+\nu} > 40$  GeV are accepted.

We present results with and without applying a jet veto. Applying a jet veto means that all events including a FS jet with  $p_{T,\text{jet}} > 100$  GeV are discarded.

## 3.3 Results on total cross sections

In Table 1 we present the LO cross sections  $\sigma^{\text{LO}}$  for different pp centre-of-mass energies  $\sqrt{s}$  and the different types of relative corrections  $\delta$  defined in (2.5). For the EW corrections resulting from the quark–antiquark channels we show results for CS and NCS observables. Results for the EW corrections originating from photon-induced channels and for the QCD corrections are listed with and without a jet veto. The different relative corrections depend only weakly on the collider energy. By far the largest effect ( $\sim 120$ – $150\%$ ) comes from the QCD corrections, even in case of a jet veto.

$pp \rightarrow l^+ \nu_l \gamma + X$			
$\sqrt{s}/\text{TeV}$	7	8	14
$\sigma^{\text{LO}}/\text{fb}$	846.53(4)	940.30(4)	1447.99(4)
$\delta_{\text{EW},q\bar{q}}^{\text{NCS}}/\%$	-3.15	-3.14	-3.15
$\delta_{\text{EW},q\bar{q}}^{\text{CS}}/\%$	-1.95	-1.94	-1.95
$\delta_{\text{EW},q\gamma}/\%$	1.04	1.10	1.30
$\delta_{\text{EW},q\gamma}^{\text{veto}}/\%$	0.74	0.76	0.84
$\delta_{\text{QCD}}/\%$	122.33(4)	128.30(5)	153.61(3)
$\delta_{\text{QCD}}^{\text{veto}}/\%$	112.47(4)	117.15(5)	135.97(9)

Table 1: Integrated cross sections and relative corrections for different LHC energies. The EW corrections to the quark–antiquark annihilation channels are provided with (CS) and without (NCS) lepton–photon recombination. EW corrections from the photon-induced channels and QCD corrections are shown with a jet veto (veto) as well as without a jet veto. The numbers in parentheses denote the integration error in the last digit. This error is negligible for the relative corrections at the given accuracy.

About two thirds of the relative QCD corrections are due to gluon-induced channels. The EW corrections to the quark–antiquark channels are about  $-2\%$  and  $-3\%$  for the CS and the NCS case, respectively. The photon-induced corrections contribute between  $0.7\%$  and  $1.3\%$  with and without a jet veto. Summing up, the total EW corrections to the integrated cross section are small and not significant for the most-recent experimental cross-section measurements. However, larger corrections show up in differential distributions, as demonstrated in the next section.

### 3.4 Results on transverse-momentum and transverse-mass distributions

In the following we present the distributions including EW and QCD corrections for various observables in separate plots. For each distribution we also show the relative EW corrections of the  $q\bar{q}$  and  $q\gamma$  channels as well as the QCD corrections with and without a jet veto.

In Fig. 9 we show results for transverse-momentum distributions. Focusing on the  $p_{T,\gamma}$  distribution of the photon (within cuts) with the highest transverse momentum we can see (Fig. 9, left, bottom) that the QCD corrections without a jet veto reach  $650\%$  for large transverse momenta (scaled down by a factor 10 in Fig. 9). This is due to the fact that new production channels occur ( $qg \rightarrow l\nu\gamma q$ ) at NLO QCD causing large corrections ( $550\%$  for large  $p_{T,\gamma}$ ). However, these large corrections come from events with hard jets, meaning that they should better be considered as part of  $W + \text{jet}$  rather than  $W + \gamma$  production. For this reason we also present results for the case of a jet veto, where all events with jets with  $p_{T,\text{jet}} > 100\text{ GeV}$  are discarded. In this case the QCD corrections become small for large  $p_{T,\gamma}$ , since the jet veto suppresses the contribution of the real QCD corrections and especially of the gluon-induced channels.

Owing to the so-called EW Sudakov logarithms the EW corrections (Fig. 9, left, top) contribute with large negative corrections in the high- $p_T$  range, though one order of magnitude smaller than the QCD corrections. The CS and the NCS cases hardly differ in the  $p_T$  distribution of the hardest photon, since the recombination of another photon collinearly emitted off the lepton only marginally effects the  $p_T$  of the hard photon. The photon-induced corrections are positive and become surprisingly large for large transverse momenta, reaching the same order of magnitude

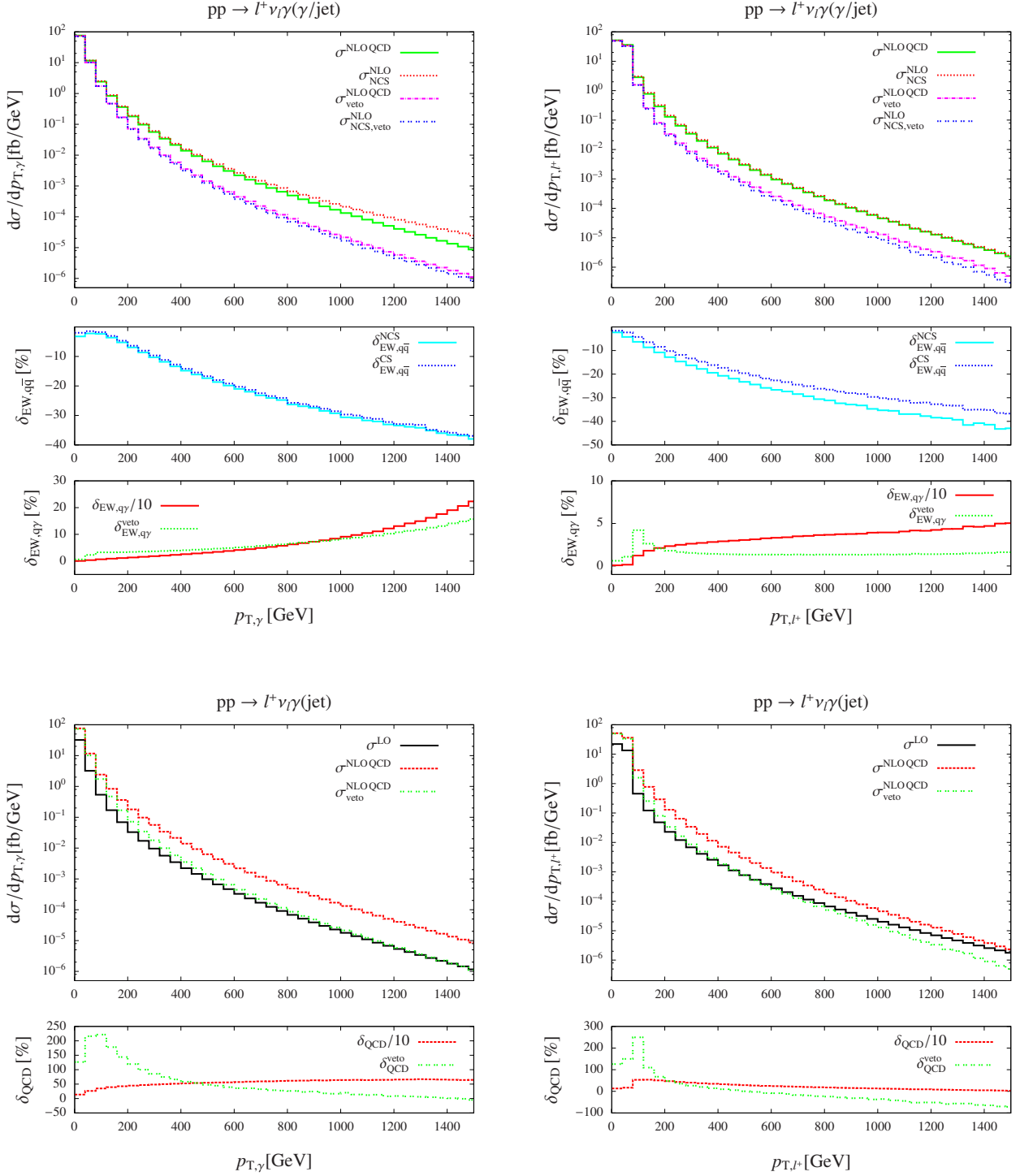


Figure 9: Distributions in the transverse momentum  $p_T$  of the photon (left) and the charged lepton (right), including EW (top) and QCD corrections (bottom). For all corrections absolute (upper box) and relative corrections (lower boxes) are shown.

as the QCD corrections. In fact in the discussion of the relative impact of the photon-induced corrections it would be more appropriate to normalize to the NLO QCD cross section, which is dominated by the new channels for hard jet emission at high scales. With this normalization the  $q\gamma$  channels still contribute some tens of percent at high  $p_{T,\gamma}$  with a rising tendency for growing  $p_{T,\gamma}$ , which can be understood by the increasing  $\gamma/g$  PDF ratio for high Bjorken- $x$  and the decrease in the strong coupling constant driven by the dynamical renormalization scale. Note, however, that the photon PDF at large Bjorken- $x$  suffers from huge uncertainties of up to 100%, so that we have to conclude that the high- $p_T$  tail of the  $p_{T,\gamma}$  distribution in the TeV range is plagued by PDF uncertainties which are of the size of the  $q\gamma$  contribution itself. Similarly to the huge QCD corrections, the large impact of the photon-induced corrections at high  $p_{T,\gamma}$  is reduced to the level of 10–15% by a jet veto, showing that those large effects are caused by hard jet emission. The jet veto, thus, helps to suppress the impact of the  $q\gamma$  contribution and the corresponding large uncertainties in the high- $p_T$  regime. After applying the veto, in fact the quark–antiquark-induced EW corrections become the dominating corrections for large transverse momenta.

In case of the  $p_T$  distribution of the charged lepton (Fig. 9, right) the QCD corrections without jet veto are large in the small- $p_T$  range and become small for large transverse momenta. In contrast the EW corrections become sizeable in the region of large transverse momenta. The corrections are roughly 5% smaller in the CS case than in the NCS case. Collinear photon emission reduces the lepton momentum, so that events with large  $p_{T,l+}$  before the emission migrate to smaller  $p_{T,l+}$ , leading to negative corrections on the falling distribution in  $p_{T,l+}$ . Photon recombination damps this effect upon shifting the major part of these migrating events back to the  $p_{T,l+}$  value before photon emission. For the case without jet veto the quark–antiquark and photon-induced EW corrections are of the same order of magnitude, but of opposite sign, and accidentally compensate each other to a large extent. In case of a jet veto the QCD corrections become large and negative for large  $p_{T,l+}$ . The large negative corrections result from the quark–antiquark-induced channels, while the corrections due to the gluon-induced channels remain small also for a jet veto. This fits well to the fact that the photon-induced corrections become negligible everywhere.

The transverse mass of the W boson and the transverse three-body mass of the W-decay products and the photon are defined by

$$M_{T,l+\nu} = \sqrt{2p_{T,l+} \cdot \not{p}_T (1 - \cos(\Delta\phi_{l+,\text{miss}}))},$$

$$M_{T,l+\nu\gamma} = \sqrt{\left(\sqrt{M_{l+\gamma}^2 + |\mathbf{p}_{T,l+} + \mathbf{p}_{T,\gamma}|^2} + \not{p}_T\right)^2 - |\mathbf{p}_{T,l+} + \mathbf{p}_{T,\gamma} + \not{p}_T|^2}, \quad (3.8)$$

where  $\Delta\phi_{l+,\text{miss}}$  is the azimuthal-angle separation between the directions of the charged lepton and the missing transverse momentum, and  $M_{l+\gamma}$  is the invariant mass of the charged lepton and the photon. The corresponding distributions are shown in Fig. 10. The smaller peak in the  $M_{T,l+\nu}$  distribution at 60 GeV appearing already at LO originates from events where the three-body invariant mass  $M_{T,l+\nu\gamma}$  lies in the resonance region and the photon is radiated by the charged FS lepton shifting the peak to smaller transverse masses. Since events with photons close to the FS lepton are discarded, a dip appears above the lower peak. As can be seen in Fig. 10, the QCD corrections are dominating the  $M_{T,l+\nu}$  distribution with and without a jet veto. At the W-mass peak, the EW corrections reach  $-4\%$  with photon recombination and  $-8\%$  in the NCS case, where the photon radiated collinear to the charged lepton carries away energy, shifting more events to regions of smaller transverse mass, where those events positively contribute to the EW corrections below the W-boson resonance. The photon-induced corrections are negligible with and without a jet veto. We note in passing that previous calculations [22, 23] of EW corrections to  $W + \gamma$  production,

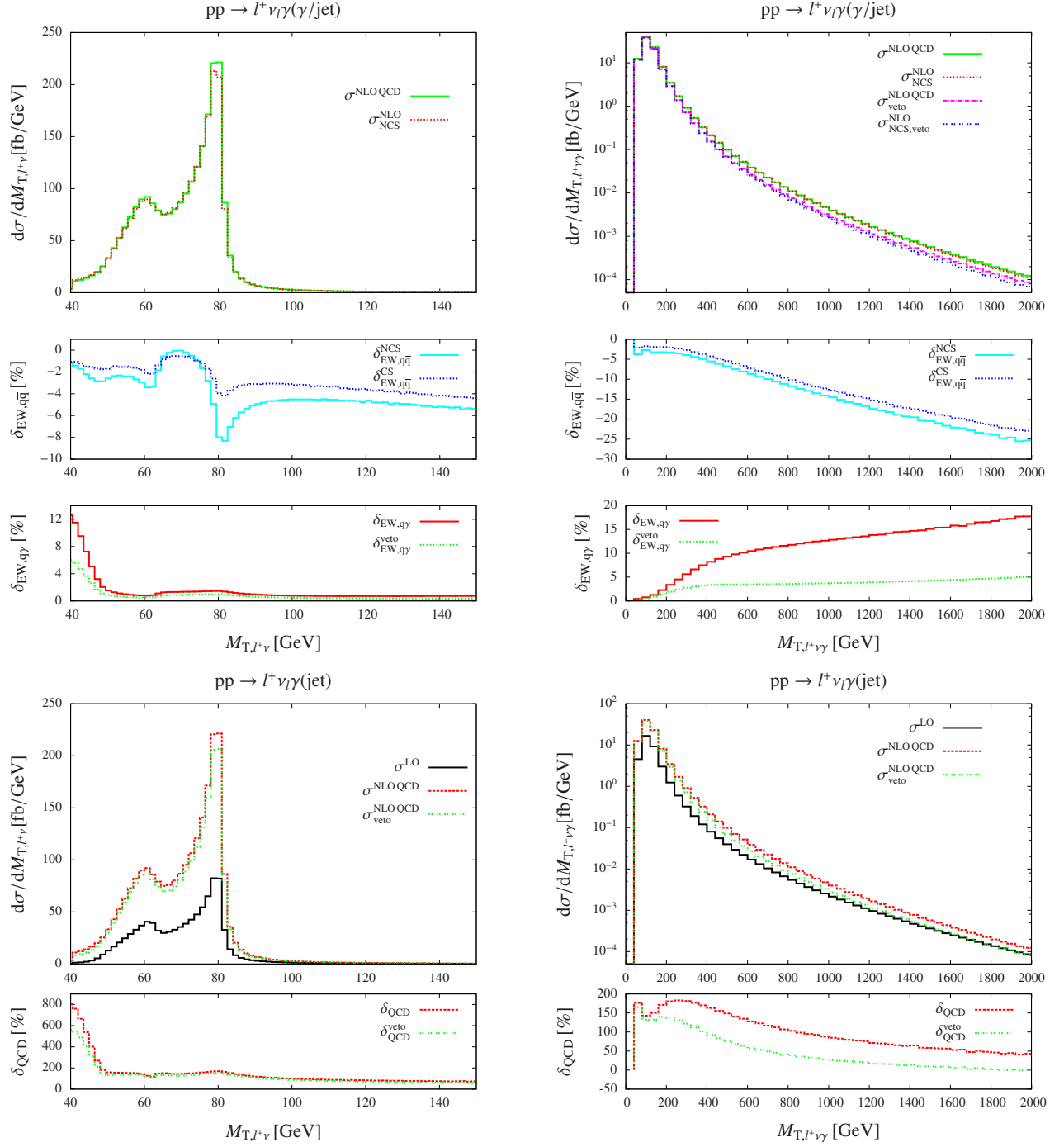


Figure 10: Distribution in the transverse mass  $M_{T,l+\nu}$  of the charged lepton and neutrino pair (left) and distribution in the transverse three-body mass  $M_{T,l+\nu\gamma}$  of the charged lepton, the neutrino, and the hardest photon (right), including EW (top) and QCD corrections (bottom). For all corrections absolute (upper box) and relative corrections (lower boxes) are shown.

which treat the W boson in pole approximation, cannot predict the range in  $M_{T,l+\nu}$  exceeding  $M_W$  which forces the W boson to go off its mass shell, while our calculation covers resonant and non-resonant regions in NLO accuracy.

We turn to the  $M_{T,l+\nu\gamma}$  distribution analysed experimentally in Ref. [5]. While the QCD corrections are dominating the region of small transverse masses, the EW and photon-induced corrections are small and have opposite signs there. In the high- $M_{T,l+\nu\gamma}$  region the situation is different. Here the QCD corrections reduce to 50% and in case of a jet veto almost tend to zero. In contrast, the EW and the photon-induced corrections without a jet veto are about 20%, but accidentally compensate each other partly. However, imposing a jet veto reduces the photon-induced corrections to 5%. As a result, the EW corrections are not compensated by the photonic corrections anymore, becoming the dominant contribution.

### 3.5 Results on rapidity and angular distributions

In Fig. 11 we show the rapidity distributions of the photon and the charged lepton. In both distributions the relative EW corrections are small and almost constant over the whole range, and thus essentially given by the corrections to the total cross section. The photon-induced contributions are of comparable magnitude, but have opposite sign so that they partially cancel the EW corrections. The QCD corrections amount to 100–180% for the rapidity distribution of the photon and to 140–160% for the one of the charged lepton and lead to sizeable shape distortions. EW corrections are completely swamped by QCD uncertainties in these observables.

In Fig. 12 we present the distributions in rapidity and the azimuthal-angle difference between the charged lepton and the photon. Note that the shape of the LO rapidity-difference distribution is highly sensitive to the chosen phase-space cuts. A potential dip at  $\Delta y_{l+\gamma} = 0$  indicating the radiation zero [7, 12, 65] is not present in the setup described in Section 3.2, but becomes visible for cuts  $p_{T,\gamma} > 20$  GeV or  $p_{T,\text{miss}} > 40$  GeV (not shown explicitly). The kink around  $40^\circ$  in the  $\Delta\phi_{l+\gamma}$  distribution is a result of the isolation cut  $R_{l+\gamma} > 0.7$  which suppresses the phase-space region with small azimuthal angle between charged lepton and photon. The EW and photon-induced corrections in Fig. 12 are at the level of 5% and affect the shape of the distributions at the level of a few per cent, whereas the QCD corrections cause large shape distortions and reach 200% in the  $\Delta y_{l+\gamma}$  and 300% in the  $\Delta\phi_{l+\gamma}$  distribution. The shape distortion in the  $\Delta y_{l+\gamma}$  distribution originates essentially from the gluon-induced corrections, which do not have a radiation zero. Especially in the rapidity-difference distribution, effects of anomalous couplings are expected to be visible as pointed out in Ref. [12]. Similarly to the rapidity distributions discussed before, the EW corrections are overwhelmed by QCD effects and the corresponding uncertainties here.

### 3.6 Results with anomalous triple gauge-boson couplings

Assuming that the SM is the low-energy limit of a more complete theory, higher-dimensional operators can be added to the SM Lagrangian to parametrize possible effects of new physics. The commonly used form of anomalous triple gauge-boson couplings (aTGCs) goes back to Ref. [66] and is based on a general parametrization of the  $WW\gamma$  and  $WWZ$  vertices (assuming W bosons coupling to conserved currents). For  $W + \gamma$  production at hadron colliders, anomalous  $WW\gamma$  couplings were, e.g., studied in Refs. [10, 12]. Following these publications we assume gauge invariance

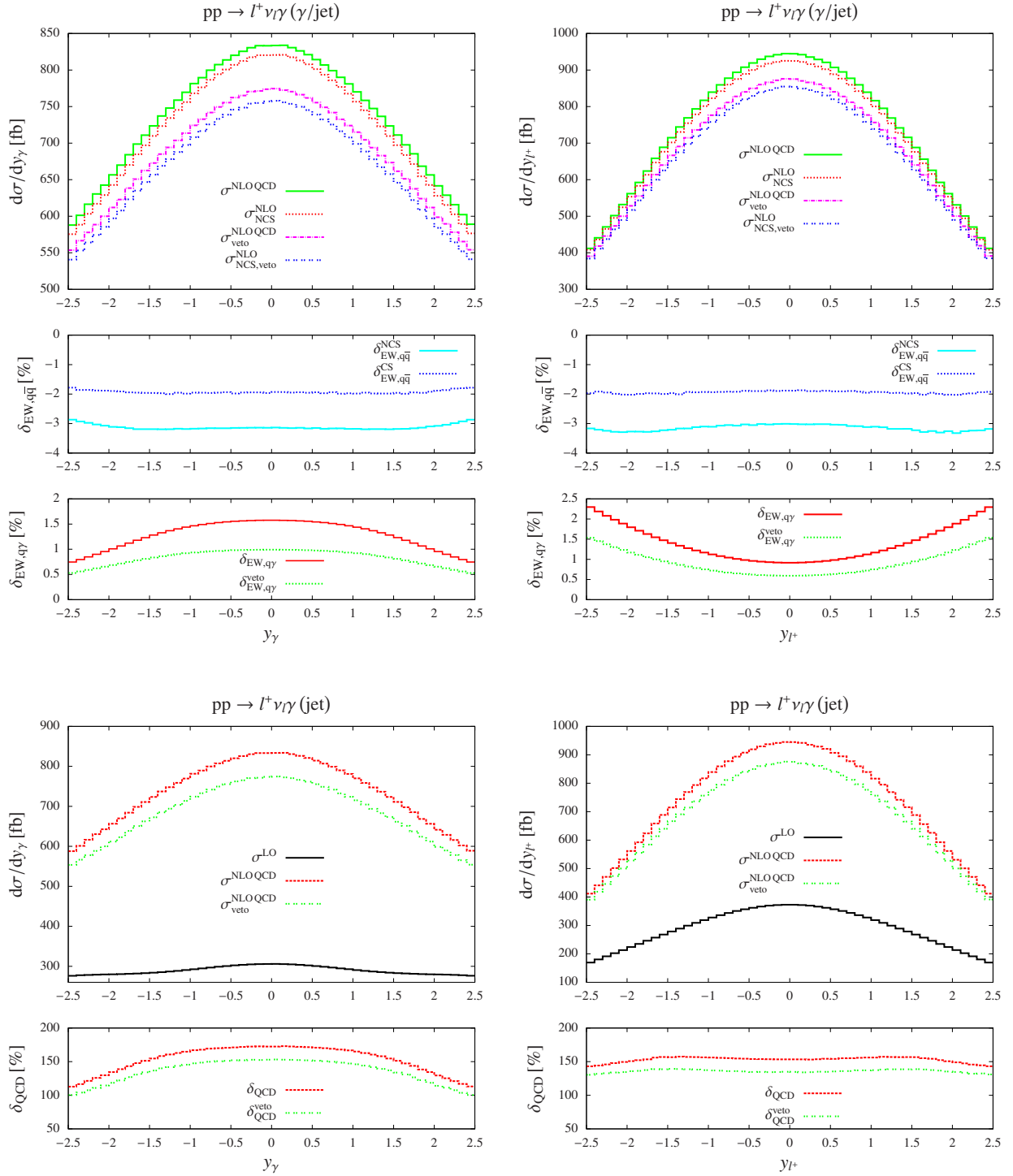


Figure 11: Distributions in the rapidity  $y_\gamma$  of the photon (left) and the rapidity  $y_{l^+}$  of the charged lepton (right), including EW (top) and QCD corrections (bottom). For all corrections absolute (upper box) and relative corrections (lower boxes) are shown.

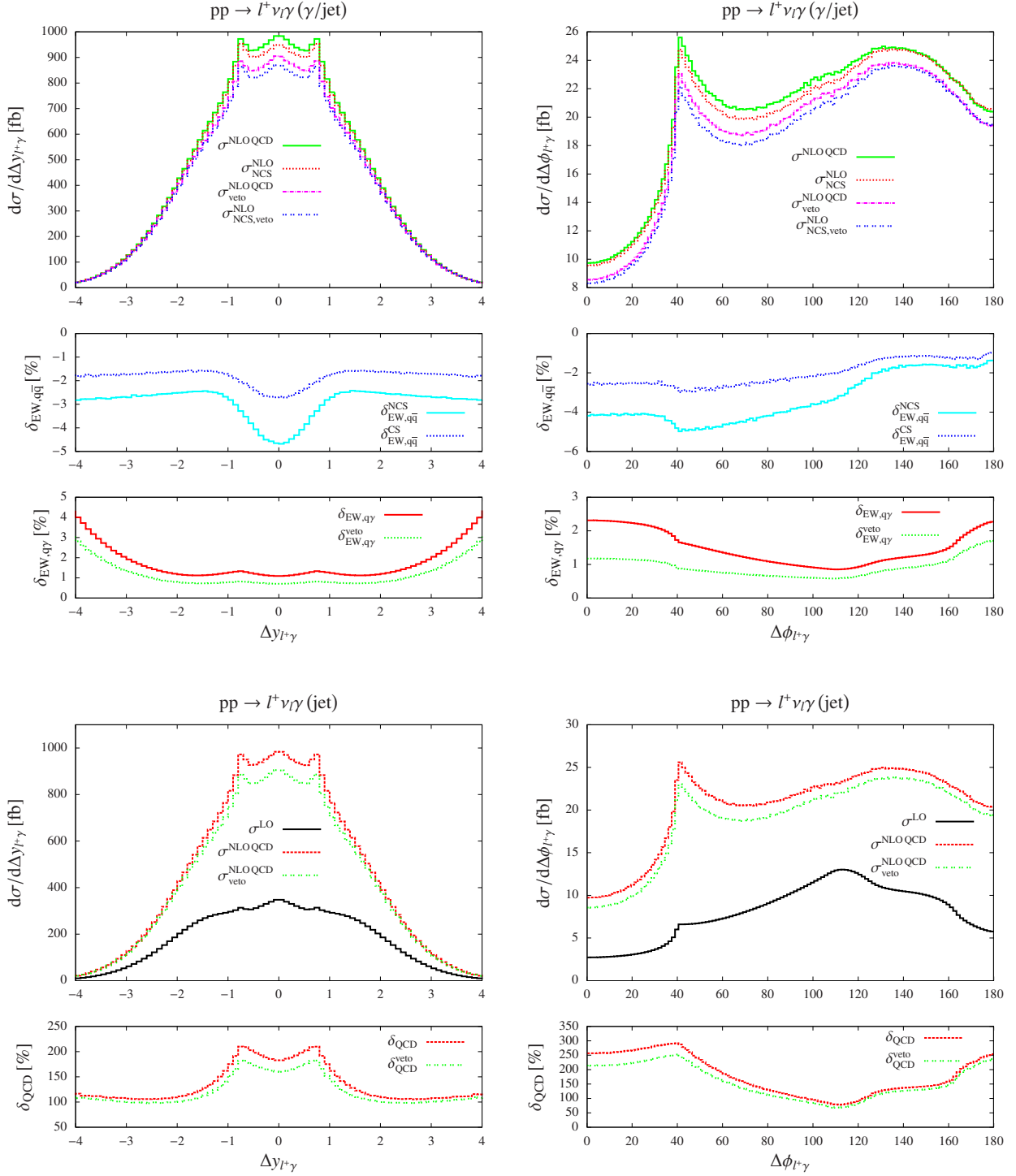


Figure 12: Distributions in the rapidity difference  $\Delta y_{l+\gamma}$  (left) and the azimuthal-angle difference  $\Delta \phi_{l+\gamma}$  (right) of the charged lepton and the photon, including EW (top) and QCD corrections (bottom). For all corrections absolute (upper box) and relative corrections (lower boxes) are shown.



as well as C and P conservation, i.e. we employ the effective vertex function

$$\Gamma_{W^+W^-\gamma,AC}^{\mu\nu\rho}(q,\bar{q},p) = e \left\{ \bar{q}^\mu g^{\nu\rho} \left( \Delta\kappa^\gamma + \lambda^\gamma \frac{q^2}{M_W^2} \right) - q^\nu g^{\mu\rho} \left( \Delta\kappa^\gamma + \lambda^\gamma \frac{\bar{q}^2}{M_W^2} \right) + (\bar{q}^\rho - q^\rho) \frac{\lambda^\gamma}{M_W^2} \left( p^\mu p^\nu - \frac{1}{2} g^{\mu\nu} p^2 \right) \right\}, \quad (3.9)$$

where  $\Delta\kappa$  and  $\lambda^\gamma$  parametrize the strengths of the anomalous couplings, and  $e$  is the electromagnetic coupling constant. The four-momenta of the incoming  $W^+$  and  $W^-$  bosons and the photon are denoted by  $q$ ,  $\bar{q}$ , and  $p$ , respectively. In contrast to Refs. [10,12,66] we consider all momenta as incoming leading to a difference by a global minus sign. The anomalous couplings spoil unitarity of the S-matrix in the limit of high energies. This problem can be bypassed by supplementing the couplings with form factors, mimicking the onset of new physics, which damps the effects of the aTGCs at high momentum transfer. We use the standard choice

$$\Delta\kappa^\gamma \rightarrow \frac{\Delta\kappa^\gamma}{\left(1 + \frac{M_{W\gamma}^2}{\Lambda^2}\right)^n}, \quad \lambda^\gamma \rightarrow \frac{\lambda^\gamma}{\left(1 + \frac{M_{W\gamma}^2}{\Lambda^2}\right)^n}, \quad (3.10)$$

where  $\Lambda$  is the scale of new physics and  $M_{W\gamma}$  is the invariant mass of the W-boson–photon system. The exponent  $n$  is chosen in such a way that the form factor is sufficient to restore unitarity. Following previous analyses we use  $n = 2$ . In order to combine the contribution of the anomalous  $WW\gamma$  coupling (AC) with the NLO corrections in a consistent way, we extend (2.4) by the relative anomalous contribution  $\delta_{AC}$ ,

$$\sigma_{AC}^{\text{NLO}} = \sigma^{\text{NLO QCD}} (1 + \delta_{EW,q\bar{q}} + \delta_{EW,q\gamma} + \delta_{AC}), \quad (3.11)$$

where  $\delta_{AC}$  is defined by

$$\delta_{AC} = \frac{\sigma_{AC}^{\text{NLO QCD}}}{\sigma^{\text{NLO QCD}}} - 1. \quad (3.12)$$

The SM cross section  $\sigma^{\text{NLO QCD}}$  is defined in (2.2), and  $\sigma_{AC}^{\text{NLO QCD}}$  is the NLO QCD cross section including the aTGC contribution. Thus,  $\delta_{AC}$  can be considered as an additional contribution to the EW correction factor in (2.4). Combining the aTGCs in a multiplicative way with the EW corrections would require an effective-field-theory approach to properly account for the fact that the effective model is non-renormalizable. In contrast, aTGCs do not conflict with the renormalization of QCD. When comparing  $\delta_{AC}$  with and without a jet veto, it should be noticed that the normalization of the two curves for  $\delta_{AC}$  is not the same, because  $\sigma^{\text{NLO QCD}}$  strongly depends on the jet veto.

Experimental limits on the parameters  $\Delta\kappa^\gamma$  and  $\lambda^\gamma$  have been updated recently in Refs. [3,4,67]. We present exemplary results for one specific point in parameter space that coincides with the present experimental limits of Ref. [67],

$$\Delta\kappa^\gamma = 0.41, \quad \lambda^\gamma = 0.074, \quad \Lambda = 2 \text{ TeV}. \quad (3.13)$$

Additionally we analyse the sensitivity on the new-physics scale by presenting results for two more values of  $\Lambda$ ,

$$\Lambda = 1 \text{ TeV}, \quad \Lambda \rightarrow \infty, \quad (3.14)$$

while  $\Delta\kappa$  and  $\lambda^\gamma$  are kept constant.

Analysing the impact of aTGCs we only present results obtained with a jet veto for the transverse-momentum distributions. In the remaining distributions they do not differ noticeably. Except for the transverse-mass distribution of the charged lepton and the neutrino, we only show relative corrections for  $\Lambda = 1\text{ TeV}$  and  $\Lambda = 2\text{ TeV}$  for the sake of clarity.

In Fig. 13 we present the transverse-momentum distributions of the photon (left) and the charged lepton (right) including aTGCs. In both distributions the effect of the anomalous couplings significantly increases with growing scale  $\Lambda$ . For  $\Lambda \rightarrow \infty$  the region of high transverse momenta receives huge contributions from the aTGCs. The differential cross sections are several orders of magnitude larger than in the SM. The effect is less dramatic for  $\Lambda = 2\text{ TeV}$ , but still of the orders of 1000% and 500% for the transverse-momentum distribution of the photon and the charged lepton, respectively. Note that  $\delta_{AC}$  and  $\delta_{AC}^{\text{veto}}$  are scaled down by a factor of 10 for  $\Lambda = 2\text{ TeV}$ . Applying a jet veto increases the impact of the aTGCs considerably, since the veto has a large effect on the differential SM cross section, but a small one in the case of aTGCs. The insensitivity of the aTGCs on the jet veto can be explained as follows: The aTGCs only have a large effect if the energy flow through the anomalous  $WW\gamma$  coupling is large. However, in case of a hard jet a substantial part of the energy is carried away by the jet. The picture is somewhat different for  $\Lambda = 1\text{ TeV}$ . In this case the relative contribution from the aTGCs has a maximum in the transverse-momentum distributions of the photon and the charged lepton around 500 GeV and 350 GeV, respectively, and decreases for larger transverse momenta. Here the effect of the form factor, suppressing the impact of the aTGCs, is directly visible. Applying a jet veto increases the relative contribution of the aTGCs for the same reason as before.

Surprisingly the impact of the aTGCs on the transverse-mass distribution of the charged lepton and the neutrino shown in Fig. 14 (left) is very small and almost becomes zero for large transverse masses. Even without a form factor the differential cross section is only three times larger than in the SM case. Note that a large two-particle transverse invariant mass  $M_{T,l+\nu}$  requires a large invariant mass  $M_{l+\nu}$ , which implies that both intermediate W bosons attached to the anomalous  $WW\gamma$  vertex are far off shell. This observation offers an explanation for the comparably small effect of aTGCs at large  $M_{T,l+\nu}$ , which are typically driven by disturbing the unitarity cancellations of the SM amplitude. For resonant W bosons these cancellations occur for longitudinally polarized W bosons with momentum  $q^\mu$  and virtuality  $q^2 \sim M_W^2$ , where the effective W polarization vector behaves like  $\varepsilon_L^\mu \sim q^\mu/\sqrt{q^2} \sim q^\mu/M_W$ . For large  $M_{T,l+\nu}$ , the W virtuality is large,  $q^2 \gg M_W^2$ , so that  $\varepsilon_L^\mu \sim q^\mu/\sqrt{q^2}$  is not enhanced by a  $1/M_W$  factor, and no large cancellations are necessary within the amplitude to avoid unitarity violations in the SM. The missing  $1/M_W$  enhancement in  $\varepsilon_L$  explains the fact that the aTGC effects are not as pronounced in the high-mass tail of  $M_{T,l+\nu}$  as compared to other scale-dependent distributions.

In contrast, a large transverse cluster mass  $M_{T,l+\nu\gamma}$  can be reached for outgoing on-shell W bosons if the photon carries away a large fraction of the momentum brought into the  $WW\gamma$  vertex by the incoming W boson, which has the large virtuality. This is the reason why the  $M_{T,l+\nu\gamma}$  distribution (see Fig. 14, right) falls off less steeply than the  $M_{T,l+\nu}$  distribution at high scales. Following the argument based on the leading behaviour of the effective longitudinal polarization vector  $\varepsilon_L$  outlined above, we expect huge aTGC effects for large  $M_{T,l+\nu\gamma}$ . In fact, for  $\Lambda \rightarrow \infty$  the differential cross section is enhanced by roughly two orders of magnitude. For  $\Lambda = 2\text{ TeV}$  the cross section is approximately ten times larger than the SM cross section in the region of large transverse masses. Note that the relative contribution of the aTGCs is scaled down by a factor of 10 for  $\Lambda = 2\text{ TeV}$ . In case of  $\Lambda = 1\text{ TeV}$  the relative anomalous contribution has a peak around 800 GeV and decreases to 30% at 2 TeV.

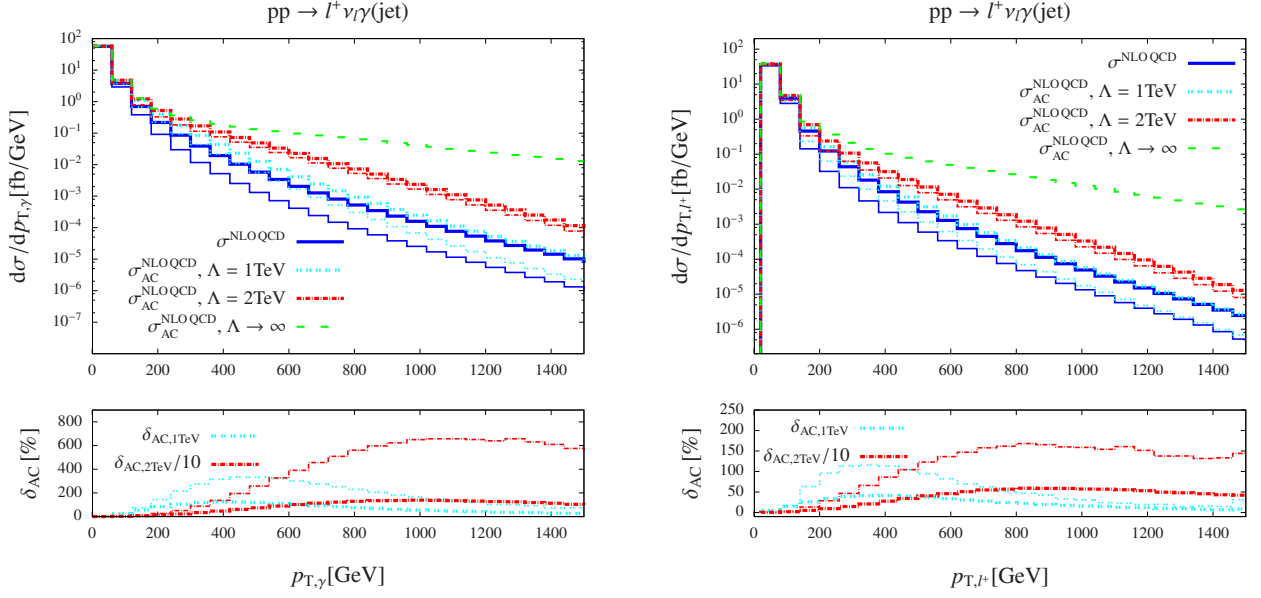


Figure 13: Absolute and relative contributions of aTGCs to the transverse-momentum distributions of the photon (left) and the charged lepton (right). Results are presented with and without a jet veto plotted with thin and thick lines, respectively.

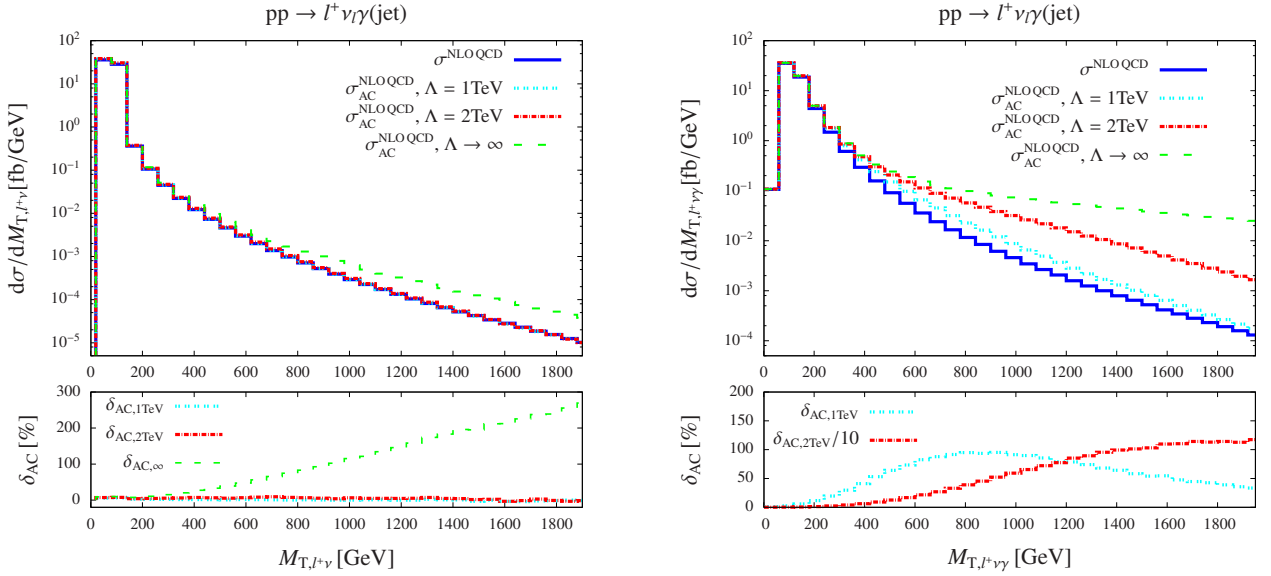


Figure 14: Absolute and relative contributions of aTGCs to the transverse-mass distribution of the charged lepton and the neutrino (left) and to the transverse three-body mass of the charged lepton, the neutrino, and the hardest photon (right).

The impact of the anomalous couplings on the rapidity distributions presented in Fig. 15 amounts to about 5% and 7% for  $\Lambda = 1 \text{ TeV}$  and  $\Lambda = 2 \text{ TeV}$ , respectively. In contrast to the rapidity distributions, the rapidity difference between the charged lepton and the photon shown in Fig. 16 (left) receives a significant shape distortion. The contribution of the aTGCs is similar for the two values of the scale  $\Lambda$  and reaches 10% around  $\Delta y_{l+\gamma} = 0$ . This can be explained by the radiation zero that appears for a stable W boson in  $W + \gamma$  production at  $\Delta y_{l+\gamma} = 0$ . This effect is, however, washed out, because the W boson decays and only the charged lepton can be detected. Additionally at NLO, QCD radiation fills the radiation zero. Since the contributions of anomalous couplings do not exhibit a radiation zero they lead to a sizeable enhancement compared to the SM prediction around  $\Delta y_{l+\gamma} = 0$ .

Focusing on the angular difference between the charged lepton and the photon (Fig. 16, right) we find a similar shape distortion for the two scales  $\Lambda = 1 \text{ TeV}$  and  $\Lambda = 2 \text{ TeV}$ . The correction induced by the aTGCs has a maximum if the angle between the photon and the charged lepton is almost  $180^\circ$ . The effect is even larger if the scale goes to infinity. Since the effect of aTGCs is enhanced at high energies, the LHC running at 14 TeV will allow to set very tight limits.

## 4 Conclusions

The production of  $W + \gamma$  final states at hadron colliders represents the ideal process to investigate the interaction of W bosons with photons at high energies. Deviations from the standard form of the  $WW\gamma$  interaction vertex, as typically predicted by Standard Model extensions, are quantified in terms of anomalous couplings which are already experimentally constrained by the analysis of W-pair production at LEP and by  $W + \gamma$  production at the Tevatron. The run 2 phase of the LHC, starting in 2015, will tighten these constraints significantly, rendering predictions for  $W + \gamma$  production at the few-per-cent level necessary.

In this paper we have improved the state-of-the-art knowledge of  $W + \gamma$  production on the side of electroweak higher-order corrections. Specifically, we have calculated the full next-to-leading-order electroweak corrections to  $W + \gamma$  production with leptonically decaying W bosons, taking into account all off-shell effects of the W boson using the complex-mass scheme and including effects originating from initial-state photons. For a phenomenologically sound definition of the  $W + \gamma$  signature, it is necessary to consistently separate hard photons from jets. To this end, we employ a quark-to-photon fragmentation function á la Glover and Morgan.

While electroweak corrections to integrated cross sections turn out to be at the level of few per cent, in line with previous predictions, they grow to several 10% in distributions where high energy scales matter. Moreover, in the high-momentum tail of the transverse-momentum distribution of the hard photon we observe a huge impact of the photon-induced channels, which inherit large uncertainties from the photon PDF at large  $x$ . In order to bring uncertainties down to the  $\sim 10\%$  level (or better) in this regime, phenomenological improvements on the photon PDF will be necessary. To some extent, a jet veto, which excludes overwhelming QCD corrections originating from hard jet emission, reduces the large size of the photon-induced channels as well. Generically, distributions in angles and rapidities receive only small uniformly distributed electroweak corrections, which are shadowed by QCD effects.

We have reproduced the next-to-leading-order QCD corrections as well and discussed the effects of anomalous triple gauge-boson couplings on various NLO-QCD-corrected distributions. For full state-of-the-art predictions the new results on electroweak corrections should be combined with the next-to-next-to-leading-order QCD corrections which have been recently presented in the literature. This combination should provide the necessary precision in predictions required for the coming data

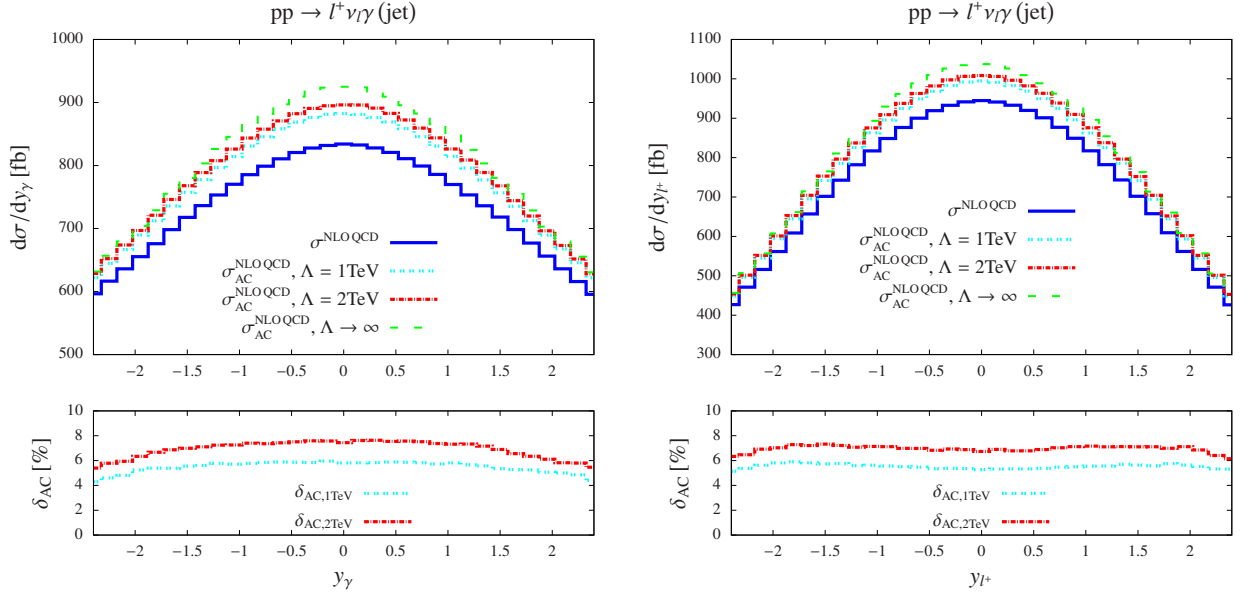


Figure 15: Absolute and relative contributions of aTGCs to the rapidity distributions of the photon (left) and the charged lepton (right).

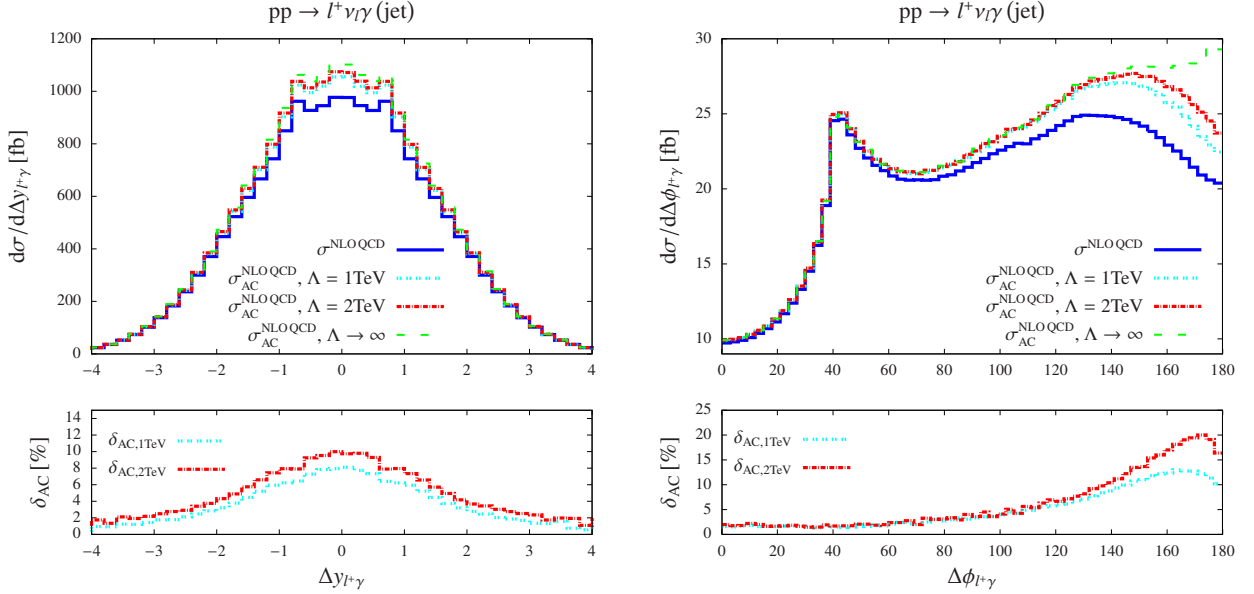


Figure 16: Absolute and relative contributions of aTGCs to the rapidity-difference distribution (left) and the azimuthal-angle-difference distribution (right) between the photon and the charged lepton.

analysis at the LHC at its design energy and luminosity.

## Acknowledgements

This project is supported by the German Research Foundation (DFG) via grant DI 784/2-1 and the research training groups GRK 1102 “Physics at Hadron Colliders” and GRK 1147 “Theoretical Astrophysics and Particle Physics”.

## References

- [1] M. S. Neubauer, *Ann.Rev.Nucl.Part.Sci.* **61** (2011) 223.
- [2] D0 Collaboration, V. M. Abazov *et al.*, *Phys.Rev.Lett.* **107** (2011) 241803, [arXiv:1109.4432 \[hep-ex\]](#).
- [3] CMS Collaboration, S. Chatrchyan *et al.*, *Phys.Rev.* **D89** (2014) 092005, [arXiv:1308.6832 \[hep-ex\]](#).
- [4] ATLAS Collaboration, G. Aad *et al.*, *Phys.Rev.* **D87** (2013) 11, 112003, [arXiv:1302.1283 \[hep-ex\]](#).
- [5] ATLAS Collaboration, G. Aad *et al.*, *Phys.Lett.* **B738** (2014) 428, [arXiv:1407.8150 \[hep-ex\]](#).
- [6] M. Schott and J. Zhu, *Int.J.Mod.Phys.* **A29** (2014) 26, 1430053, [arXiv:1406.7731 \[hep-ex\]](#).
- [7] R. Brown, D. Sahdev, and K. Mikaelian, *Phys.Rev.* **D20** (1979) 1164.
- [8] J. Smith, D. Thomas, and W. van Neerven, *Z.Phys.* **C44** (1989) 267.
- [9] J. Ohnemus, *Phys.Rev.* **D47** (1993) 940.
- [10] U. Baur, T. Han, and J. Ohnemus, *Phys.Rev.* **D48** (1993) 5140, [arXiv:hep-ph/9305314 \[hep-ph\]](#).
- [11] L. J. Dixon, Z. Kunszt, and A. Signer, *Nucl.Phys.* **B531** (1998) 3, [arXiv:hep-ph/9803250 \[hep-ph\]](#).
- [12] D. De Florian and A. Signer, *Eur.Phys.J.* **C16** (2000) 105, [arXiv:hep-ph/0002138 \[hep-ph\]](#).
- [13] J. M. Campbell, R. K. Ellis, and C. Williams, *JHEP* **1107** (2011) 018, [arXiv:1105.0020 \[hep-ph\]](#).
- [14] K. Adamson, D. de Florian, and A. Signer, *Phys.Rev.* **D65** (2002) 094041, [arXiv:hep-ph/0202132 \[hep-ph\]](#).
- [15] M. Grazzini, *PoS LL2014* (2014) 027, [arXiv:1407.1618 \[hep-ph\]](#).
- [16] L. Barze *et al.*, *JHEP* **12** (2014) 039, [arXiv:1408.5766 \[hep-ph\]](#).
- [17] W. Beenakker, A. Denner, S. Dittmaier, R. Mertig, and T. Sack, *Nucl.Phys.* **B410** (1993) 245.

- [18] M. Beccaria, G. Montagna, F. Piccinini, F. Renard, and C. Verzegnassi, Phys.Rev. **D58** (1998) 093014, [arXiv:hep-ph/9805250](#) [hep-ph].
- [19] P. Ciafaloni and D. Comelli, Phys.Lett. **B446** (1999) 278, [arXiv:hep-ph/9809321](#) [hep-ph].
- [20] J. H. Kühn and A. Penin, [arXiv:hep-ph/9906545](#) [hep-ph].
- [21] A. Denner and S. Pozzorini, Eur.Phys.J. **C18** (2001) 461, [arXiv:hep-ph/0010201](#) [hep-ph].
- [22] E. Accomando, A. Denner, and S. Pozzorini, Phys.Rev. **D65** (2002) 073003, [arXiv:hep-ph/0110114](#) [hep-ph].
- [23] E. Accomando, A. Denner, and C. Meier, Eur.Phys.J. **C47** (2006) 125, [arXiv:hep-ph/0509234](#) [hep-ph].
- [24] E. W. N. Glover and A. G. Morgan, Z. Phys. **C62** (1994) 311.
- [25] E. W. N. Glover and A. G. Morgan, Phys. Lett. **B334** (1994) 208.
- [26] S. Dittmaier, Phys.Rev. **D59** (1998) 016007, [arXiv:hep-ph/9805445](#) [hep-ph].
- [27] A. Denner, S. Dittmaier, and L. Hofer, PoS **LL2014** (2014) 071, [arXiv:1407.0087](#) [hep-ph].
- [28] A. Denner and S. Dittmaier, Nucl.Phys. **B658** (2003) 175, [arXiv:hep-ph/0212259](#) [hep-ph].
- [29] A. Denner and S. Dittmaier, Nucl.Phys. **B734** (2006) 62, [arXiv:hep-ph/0509141](#) [hep-ph].
- [30] A. Denner and S. Dittmaier, Nucl.Phys. **B844** (2011) 199, [arXiv:1005.2076](#) [hep-ph].
- [31] T. Hahn, Comput.Phys.Comm. **140** (2001) 418, [arXiv:hep-ph/0012260](#) [hep-ph].
- [32] T. Hahn and C. Schappacher, Comput.Phys.Comm. **143** (2002) 54, [arXiv:hep-ph/0105349](#) [hep-ph].
- [33] T. Hahn and M. Perez-Victoria, Comput.Phys.Comm. **118** (1999) 153, [arXiv:hep-ph/9807565](#) [hep-ph].
- [34] S. Dittmaier and M. Roth, Nucl.Phys. **B642** (2002) 307, [arXiv:hep-ph/0206070](#) [hep-ph].
- [35] G. P. Lepage, J.Comput.Phys. **27** (1978) 192.
- [36] G. P. Lepage. CLNS-80/447.
- [37] J. Küblbeck, M. Böhm, and A. Denner, Comput.Phys.Comm. **60** (1990) 165.
- [38] A. Denner, S. Dittmaier, M. Roth, and D. Wackerroth, Nucl.Phys. **B560** (1999) 33, [arXiv:hep-ph/9904472](#) [hep-ph].
- [39] A. Denner, S. Dittmaier, M. Roth, and L. Wieders, Nucl.Phys. **B724** (2005) 247, [arXiv:hep-ph/0505042](#) [hep-ph].

- [40] A. Denner and S. Dittmaier, Nucl.Phys.Proc.Suppl. **160** (2006) 22, [arXiv:hep-ph/0605312](#) [hep-ph].
- [41] A. Denner, Fortsch.Phys. **41** (1993) 307, [arXiv:0709.1075](#) [hep-ph].
- [42] D. Melrose, Nuovo Cim. **40** (1965) 181.
- [43] G. Passarino and M. Veltman, Nucl.Phys. **B160** (1979) 151.
- [44] G. 't Hooft and M. Veltman, Nucl.Phys. **B153** (1979) 365.
- [45] A. Denner, U. Nierste, and R. Scharf, Nucl.Phys. **B367** (1991) 637.
- [46] W. Beenakker and A. Denner, Nucl.Phys. **B338** (1990) 349.
- [47] S. Catani and M. H. Seymour, Nucl. Phys. **B485** (1997) 291, [arXiv:hep-ph/9605323](#).
- [48] S. Catani, S. Dittmaier, M. H. Seymour, and Z. Trocsanyi, Nucl.Phys. **B627** (2002) 189, [arXiv:hep-ph/0201036](#) [hep-ph].
- [49] S. Dittmaier, Nucl.Phys. **B565** (2000) 69, [arXiv:hep-ph/9904440](#) [hep-ph].
- [50] S. Dittmaier, A. Kabelschacht, and T. Kasprzik, Nucl.Phys. **B800** (2008) 146, [arXiv:0802.1405](#) [hep-ph].
- [51] U. Baur, S. Keller, and D. Wackeroth, Phys.Rev. **D59** (1999) 013002, [arXiv:hep-ph/9807417](#) [hep-ph].
- [52] S. Dittmaier and M. Huber, JHEP **1001** (2010) 060, [arXiv:0911.2329](#) [hep-ph].
- [53] NNPDF Collaboration, R. D. Ball *et al.*, Nucl.Phys. **B877** (2013) 290, [arXiv:1308.0598](#) [hep-ph].
- [54] K.-P. Diener, S. Dittmaier, and W. Hollik, Phys.Rev. **D72** (2005) 093002, [arXiv:hep-ph/0509084](#) [hep-ph].
- [55] T. Kinoshita, J.Math.Phys. **3** (1962) 650.
- [56] T. Lee and M. Nauenberg, Phys.Rev. **133** (1964) B1549.
- [57] A. Denner, S. Dittmaier, T. Kasprzik, and A. Mück, JHEP **0908** (2009) 075, [arXiv:0906.1656](#) [hep-ph].
- [58] ALEPH Collaboration, D. Buskulic *et al.*, Z. Phys. **C69** (1996) 365.
- [59] A. Denner, S. Dittmaier, T. Gehrmann, and C. Kurz, Nucl.Phys. **B836** (2010) 37, [arXiv:1003.0986](#) [hep-ph].
- [60] Particle Data Group, J. Beringer *et al.*, Phys.Rev. **D86** (2012) 010001.
- [61] J. Butterworth *et al.*, [arXiv:1405.1067](#) [hep-ph].
- [62] D. Bardin, A. Leike, T. Riemann, and M. Sachwitz, Phys.Lett. **B206** (1988) 539.
- [63] L. J. Dixon, Z. Kunszt, and A. Signer, Phys.Rev. **D60** (1999) 114037, [arXiv:hep-ph/9907305](#) [hep-ph].



- [64] S. Haywood *et al.*, [arXiv:hep-ph/0003275](#) [hep-ph].
- [65] U. Baur, S. Errede, and G. L. Landsberg, *Phys.Rev.* **D50** (1994) 1917, [arXiv:hep-ph/9402282](#) [hep-ph].
- [66] K. Hagiwara, R. D. Peccei, D. Zeppenfeld, and K. Hikasa, *Nucl.Phys.* **B282** (1987) 253.
- [67] ATLAS Collaboration, G. Aad *et al.*, *Phys.Lett.* **B717** (2012) 49, [arXiv:1205.2531](#) [hep-ex].